Development of a Versatile Battery Simulator for Testing Power Electronics Systems Across Multiple Battery Chemistries

M.Tech Thesis

by

Sandeep Sarkar

CENTER FOR ELECTRIC VEHICLE AND INTELLIGENT TRANSPORT SYSTEM

INDIAN INSTITUTE OF TECHNOLOGY INDORE

May 2025

Development of a Versatile Battery Simulator for Testing Power Electronics Systems Across Multiple Battery Chemistries

A THESIS

Submitted in partial fulfillment of the

requirements for the award of the degree of

Master of Technology

by

Sandeep Sarkar

2302106005

CENTER FOR ELECTRIC VEHICLE AND

INTELLIGENT TRANSPORT SYSTEM

INDIAN INSTITUTE OF TECHNOLOGY

INDORE

May 2025

INDIAN INSTITUTE OF TECHNOLOGY INDORE

CANDIDATE’S DECLARATION

I hereby certify that the work which is being presented in the thesis entitled **Development of a Versatile Battery Simulator for Testing of Power Electronics Systems Across Multiple Battery Chemistries** in the **partial fulfillment of the requirements for the award of the degree of MASTER OF TECHNOLOGY** and submitted in the **CENTER FOR ELECTRIC VEHICLE AND INTELLIGENT TRANSPORT SYSTEMS**, **Indian Institute of Technology Indore**, is an authentic record of my own work carried out during the time period from **July 2024 to May 2025** under the supervision of **Dr. Amod C. Umarikar, Professor, Electrical Engineering**.

The matter presented in this thesis has not been submitted by me for the award of any other degree of this or any other institute.

Sandeep Sarkar 28.05.2025

Signature of the Student with Date

(Sandeep Sarkar)

……

This is to certify that the above statement made by the candidate is correct to the best of my knowledge.

29/05/2025

Signature of Thesis Supervisor with Date

(Dr. Amod C. Umarikar)

……

ACKNOWLEDGEMENT

I would like to express my profound gratitude to my project supervisor, **Dr. Amod C. Umarikar**, for his invaluable guidance, continuous encouragement, and insightful feedback throughout the course of my M.Tech project. His unwavering support and constructive suggestions have been instrumental in shaping the direction and quality of this work.

I am sincerely thankful to him for providing me the opportunity to undertake the project titled **"Development of a Versatile Battery Simulator for Testing of Power Electronics Systems Across Multiple Battery Chemistries"** within the department premises, in partial fulfillment of the requirements for the degree of **Master of Technology (M.Tech)**.

I also extend my gratitude to my project collaborators and all individuals who have contributed their time, expertise, and support during the course of this project. Their assistance has been greatly appreciated. Furthermore, I wish to thank all the faculty members of the department for their academic support and guidance, both direct and indirect, which have been crucial throughout my M.Tech journey. Lastly, I am deeply grateful to my friends for their constant motivation, cooperation, and moral support, which have played a vital role during this academic endeavor.

Dedicated to My Family

DEDICATION

I dedicate this thesis to my beloved parents, whose unwavering love, prayers, and sacrifices have laid the foundation for all my achievements. Their steadfast belief in my abilities has been my greatest source of strength throughout this journey.

To my mentor and supervisor, Dr. Amod C. Umarikar, I extend my deepest respect and gratitude for his insightful guidance, encouragement, and intellectual support, which have been instrumental in shaping the direction and success of this work.

I also dedicate this work to my friends and well-wishers, whose consistent support and motivation have helped me persevere through every challenge.

To the esteemed faculty and staff of the Center for Electric Vehicle and Intelligent Transport Systems, IIT Indore, I offer sincere thanks for their valuable contributions, which have enriched this academic experience.
Finally, I dedicate this thesis to all individuals who dare to dream and pursue their goals with passion, resilience, and determination.

ABSTRACT

A Battery Emulator (BE) is a real-time hardware platform designed to replicate the electrical behavior of real batteries, thereby facilitating safe, flexible, and cost-effective testing of power electronic systems. Battery emulators are instrumental in accelerating research and development in domains such as Electric Vehicles (EVs), Battery Management Systems (BMS), and Renewable Energy System (RES) integration, by mitigating the safety risks, variability, and financial constraints associated with physical batteries.

This thesis presents the design and implementation of a versatile battery simulator integrated with a bidirectional DC-DC converter. The system is capable of accurately emulating both charging and discharging behaviors across multiple battery chemistries. At its core lies an equivalent circuit-based lithium-ion battery model, selected and validated through rigorous simulation studies conducted in MATLAB/Simulink.

The developed emulator is designed for seamless integration into both grid-connected and standalone configurations, enabling comprehensive evaluation of battery performance under a wide range of operating scenarios. Simulation and experimental validation confirm that the proposed emulator effectively replicates real battery dynamics, positioning it as a valuable tool for modern energy storage research, system development, and testing.

Contents

List of Figures

List of Tables

Chapter 1

Introduction

With the increasing integration of renewable energy sources (RES) in modern power systems, driven by the global pursuit of sustainable and cleaner energy, new challenges have emerged for grid stability and reliability. The inherently intermittent and unpredictable nature of RESs, such as solar and wind, significantly burdens existing electrical infrastructure, especially in regions where the grid is already weak or underdeveloped. In such scenarios, maintaining voltage and frequency stability becomes increasingly complex, and the risk of grid instability or blackout rises. [16]

Grid Energy Storage Systems (GESSs) have been deployed to mitigate these challenges to absorb fluctuations, smooth power output, and support grid reliability. Among the various available storage technologies, Lithium-ion Batteries (LIBs) have emerged as one of the most promising solutions due to their high energy density, efficiency, and scalability. However, despite their advantages, the high cost of LIBs presents a significant barrier to widespread deployment, particularly for research institutions, universities, and even industries aiming to evaluate and test advanced Power Electronic Systems and Battery Management Systems (BMS). [3] [17]

A practical and cost-effective solution to address this limitation is using Battery

Emulators (BEs)—real-time platforms designed to replicate the dynamic electrical behavior of real batteries under various operating conditions. These systems allow researchers and engineers to safely test and validate power electronic converters, control strategies, and BMS algorithms without the risk, cost, or variability associated with physical batteries.

1.1 Scope of the Study

This thesis focuses on the development of a versatile battery emulator integrated with a bidirectional DC-DC converter, capable of emulating both charging and discharging profiles across multiple battery chemistries. The core of the emulator is based on an equivalent circuit model of a Li-ion battery, selected and validated through extensive simulation studies conducted in MATLAB/Simulink. Unlike some previous works that rely on Digital Signal Processors (DSPs) or embedded C-code implementations, this study emphasizes a simulation-driven approach for proof-of-concept development, prioritizing flexibility and adaptability over embedded implementation.

The emulator is designed to support integration in both grid-connected and standalone systems, enabling realistic and reproducible testing of power electronic hardware and control systems under a variety of battery operating conditions.

1.2 Thesis Objectives

The key objectives of this thesis are:

1. To analyze and summarize the key characteristics and operational behavior of Lithium-ion and other battery chemistries relevant to energy storage.

2. To review current battery modeling approaches, with a focus on circuit-based models suitable for emulator applications.
3. To develop an equivalent circuit-based battery model in MATLAB/Simulink that can be adapted for various battery chemistries and operating conditions.
4. To design and implement a versatile battery emulator integrated with a bidirectional DC-DC converter to support both charging and discharging emulation.
5. To validate the performance of the proposed emulator through simulation and experimental testing using representative use cases.

1.3 Thesis Outline

The remainder of this thesis is organized as follows:

- **Chapter 2** presents the motivation behind the adoption of Lithium-Ion Batteries (LIBs) in electric vehicles and energy storage systems. It highlights the limitations of conventional energy storage and the advantages offered by LIBs in modern applications.[2]
- **Chapter 3** provides a detailed background on Lithium-Ion Batteries, including a comparison of various LIB chemistries. This chapter establishes the foundational knowledge necessary for understanding their selection and behavior in emulation platforms.
- **Chapter 4** discusses key battery phenomena such as charging/discharging characteristics, C-rate effects, and thermal behavior. It also introduces basic principles of battery management, setting the stage for accurate battery emulation and control.

- **Chapter 5** reviews the existing literature on battery modeling approaches, focusing on equivalent circuit models and the integration of experimental results. The chapter also analyzes the accuracy and limitations of various modeling strategies for emulation purposes.

- **Chapter 6** presents the hardware topology and circuit design of the battery emulator developed in this work. It includes the bidirectional DC-DC converter architecture, control logic, and key design considerations for enabling both charging and discharging profiles.

- **Chapter 7** concludes the thesis by summarizing the main contributions, discussing the limitations of the current emulator system, and outlining future directions for improving model fidelity and expanding the emulator's functionality.

Chapter 2

Motivation for Lithium-Ion Batteries (LIBs)

2.1 LIBs vs Other Grid Energy Storage Systems (GESSs)

Among the numerous Grid Energy Storage Systems (GESSs) developed to date, Battery Energy Storage Systems (BESSs), particularly Lithium-Ion Batteries (LIBs), are regarded as the most promising solution. One of the primary advantages of LIBs is their broad operational range—from milliseconds to several hours—at relatively high power levels. This enables their use in both high-power and high-energy applications, as illustrated in Fig. 2.1.

Unlike Pumped Storage Hydro (PSH) and Compressed Air Energy Storage (CAES), LIBs can be installed virtually anywhere on the grid due to their compact and modular nature. In contrast, PSH and CAES are limited by geographical and topological constraints and involve high capital investments and lengthy planning procedures [1].

Although technologies such as Supercapacitors (EDLCs) and Flywheels (FWs)

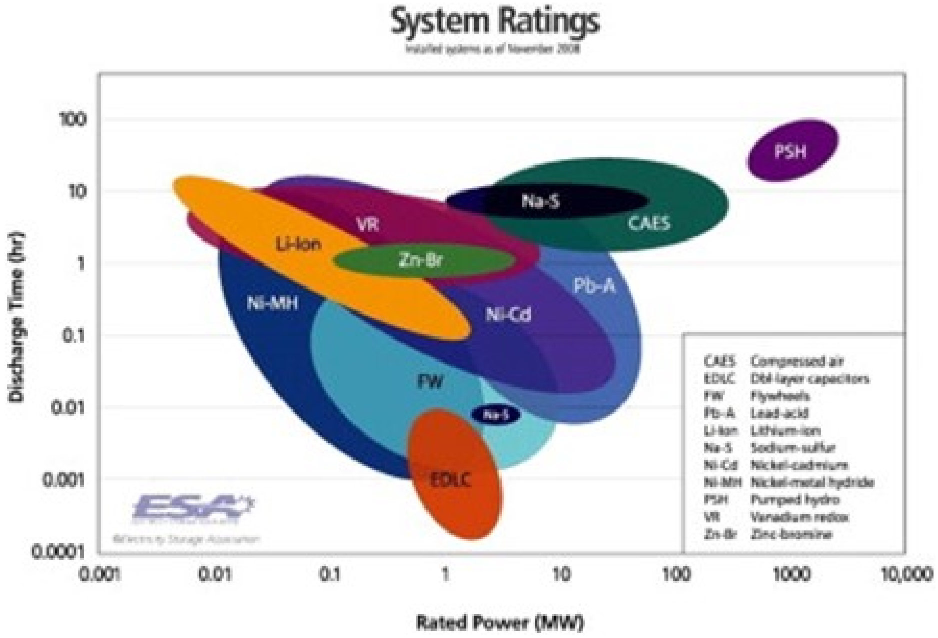

Figure 2.1: Comparison of energy storage technologies - Discharge time vs Rated power [1]

offer faster response times, they suffer from high self-discharge rates, limiting their utility in high-energy applications [1]. LIBs, being part of the BESS category, also benefit from distributed deployment capabilities. Figure 2.2 outlines various grid-based applications of distributed GESSs.

2.2 LIBs vs Other BESS Technologies

LIBs encompass a variety of chemistries, which will be discussed in Chapter 3. Nevertheless, their superiority over other BESS technologies is widely acknowledged due to the following attributes. [3] [18] [7]

- High energy density and lightweight structure
- Long cycle life
- Low self-discharge rate

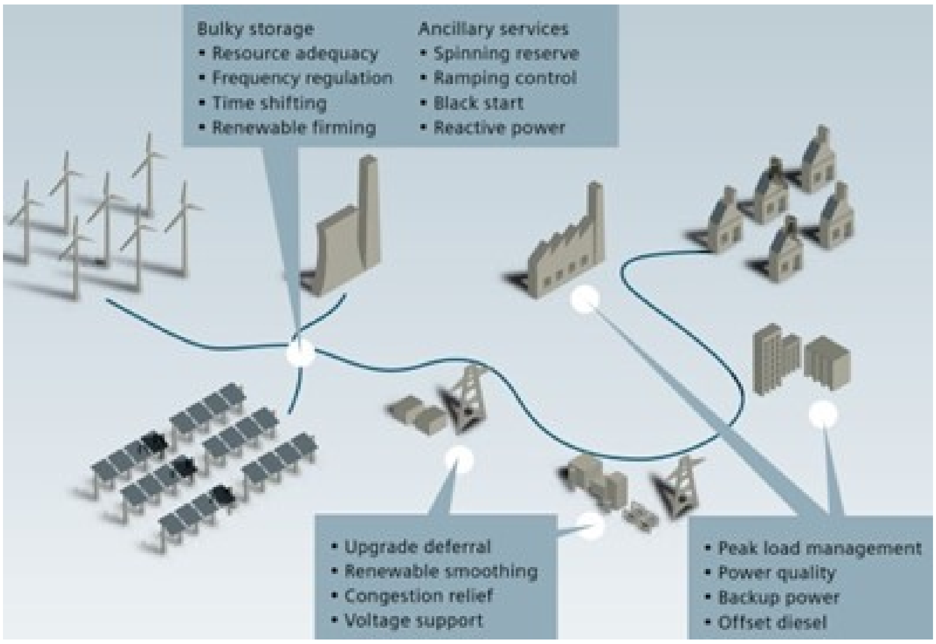

Figure 2.2: Applications of distributed GESSs. [2]

- High charge/discharge capability

This dominance can also be seen in Figure 2.3, where specific power vs specific energy is depicted for various energy storage technologies at the cell level, as they are considered for the automotive industry. It should be noted that although the application is different, the battery cells are, in most cases, the same. Hence, more similar examples in which the automotive industry crosses with the grid energy storage industry will be seen throughout the report. From another perspective, the advantages of LIBs can be seen in Figure 2.4.

2.3 Overview of Alternative BESS Technologies

Nickel-Metal Hydride (Ni-MH)

Ni-MH batteries offer a broad operating temperature range $-30°C$ to $+75°C$ and are inherently safer than LIBs. They have demonstrated reliability in automotive

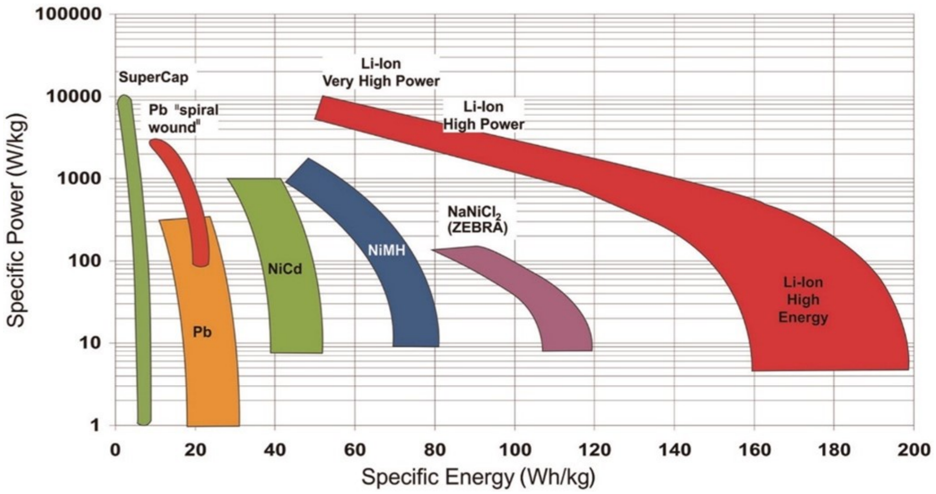

Figure 2.3: Comparison of energy storage technologies at the cell level for automotive applications [3]

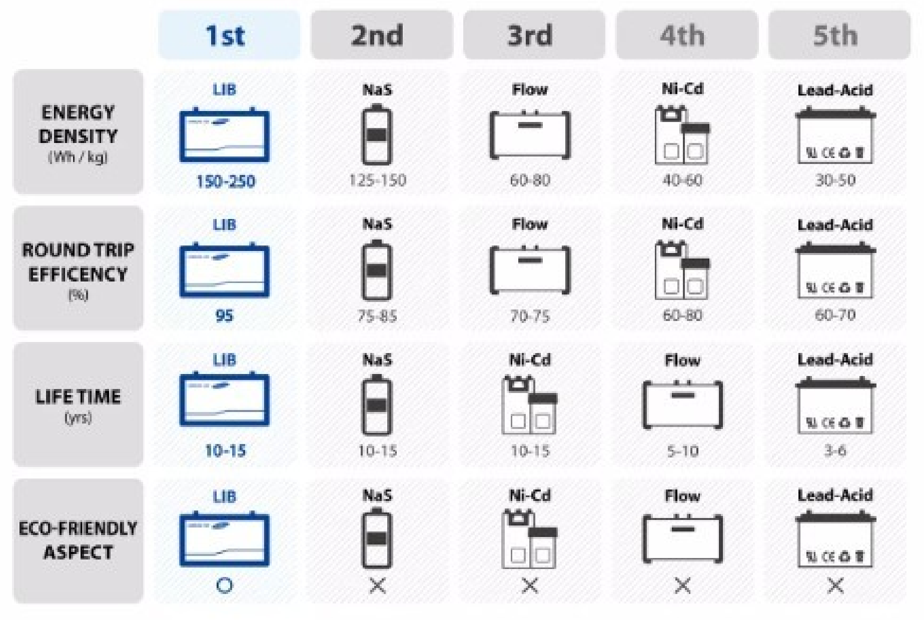

	1st	2nd	3rd	4th	5th
ENERGY DENSITY (Wh / kg)	LIB 150-250	NaS 125-150	Flow 60-80	Ni-Cd 40-60	Lead-Acid 30-50
ROUND TRIP EFFICENCY (%)	LIB 95	NaS 75-85	Flow 70-75	Ni-Cd 60-80	Lead-Acid 60-70
LIFE TIME (yrs)	LIB 10-15	NaS 10-15	Ni-Cd 10-15	Flow 5-10	Lead-Acid 3-6
ECO-FRIENDLY ASPECT	LIB ○	NaS ×	Ni-Cd ×	Flow ×	Lead-Acid ×

Figure 2.4: General comparison of BESSs. [4]

applications. However, their high self-discharge rate, memory effect, lower energy density (approximately 60% of LIBs), and the high cost of nickel restrict their use in large-scale GESSs. [3] [1] [19]

Lead-Acid (Pb-A)

Lead-acid batteries are among the oldest and most mature technologies. They are used in several large-scale BESS applications, such as the 10MW/40MWh system in California. However, their disadvantages include low energy density, short cycle life, and environmental concerns due to lead toxicity [1]. Figure 2.5 provides a comparative overview of Pb-A and LIB technologies [4].

Figure 2.5: Comparison of Pb-A and LIB technologies. [4]

Sodium-Sulphur (Na-S)

Na-S batteries, developed initially for automotive use in the 1960s, are now primarily utilized in GESSs. Operating at temperatures between 300°C and 350°C, they offer high energy density, long cycle life, and significant peak power capability. Despite these advantages, the high operational temperature and the reactivity of sodium pose safety risks. Moreover, in the event of system shutdowns, energy losses due to heat dissipation can result in up to 20% self-discharge per day. [1] [20]

Vanadium Redox (VR) Flow Batteries

Vanadium Redox batteries, introduced in the early 1980s, are flow batteries with two separate liquid electrolytes stored in tanks and circulated through a membrane to produce a voltage of 1.4–1.6 V. Their decoupled energy and power characteristics allow scalable design. While they feature excellent cycle life, moderate cost, and no self-discharge, their limited operating temperature range ($10°C$ to $35°C$) and low technology maturity remain concerns. Ongoing research focuses on extending the temperature range, improving energy/power density, and advancing membrane technologies [1]. A schematic of the VR battery system is shown in Figure 2.6.

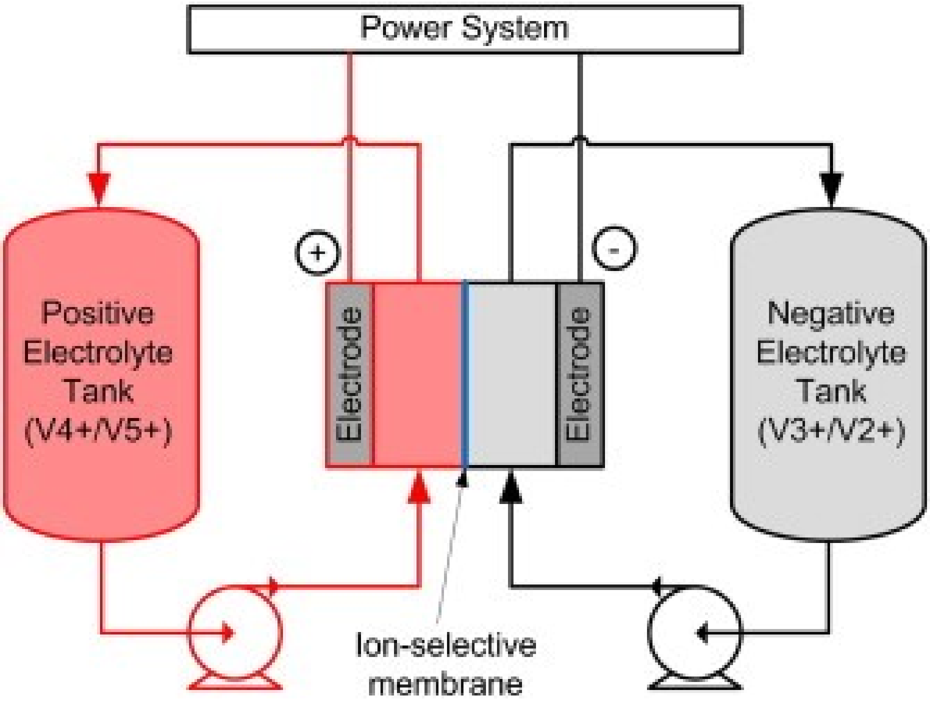

Figure 2.6: Schematic of Vanadium Redox (VR) Flow Battery System [1]

2.4 Cost Outlook for LIBs

Historically, the high cost of LIBs, driven by limited lithium availability and small-scale production, restricted their adoption to consumer electronics. However, in recent years, LIB deployment has expanded into the automotive and energy sectors. [18] [7]

Projections indicate significant cost reductions due to mass production and technological advancements. Estimates suggest a decrease from approximately Rs. 32,500/kWh in 2015 to Rs. 13,000/kWh by 2020, with some manufacturers like A123 Systems aiming for Rs. 8,500/kWh within the same timeframe. [21] [22] Fig. 3.5 illustrates the expected cost decline as a function of electric vehicle (EV) production scale. [5]

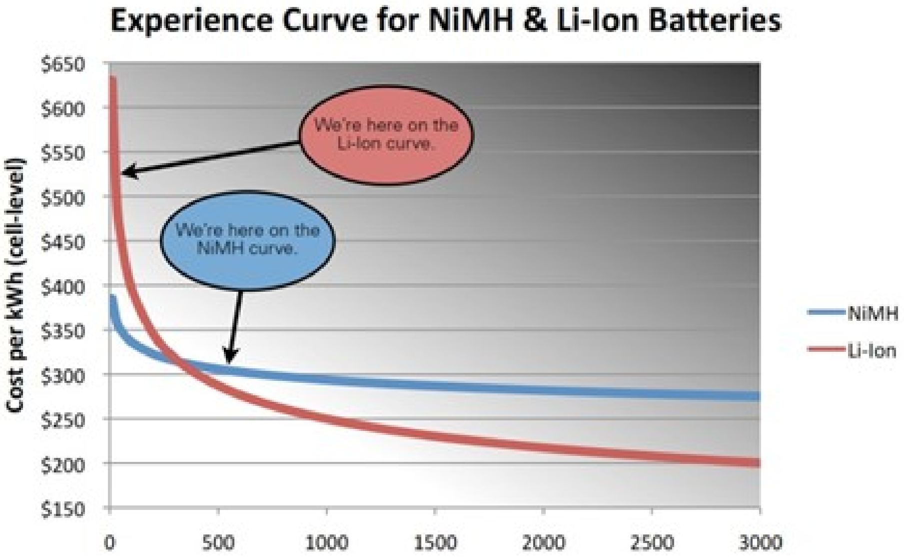

Figure 2.7: Projected cost decline of LIBs with EV production scale [5]

Chapter 3

Background for Lithium-Ion Batteries (LIBs)

3.1 Introduction to Lithium-Based Battery Technologies

Lithium-based batteries represent the forefront of energy storage technologies due to their superior electrochemical characteristics. These batteries are categorized into two primary types: lithium-metal batteries and lithium-ion batteries. The classification depends on the anode material—lithium-metal batteries employ lithium metal as the anode, while lithium-ion batteries use a carbon-based anode such as graphite. Among these, lithium-ion batteries (LIBs) have become the most commercially successful due to their optimal balance of energy density, safety, and cycle life. In recent years, the deployment of LIBs has expanded beyond consumer electronics into electric mobility, stationary storage systems, and grid support applications. [7]

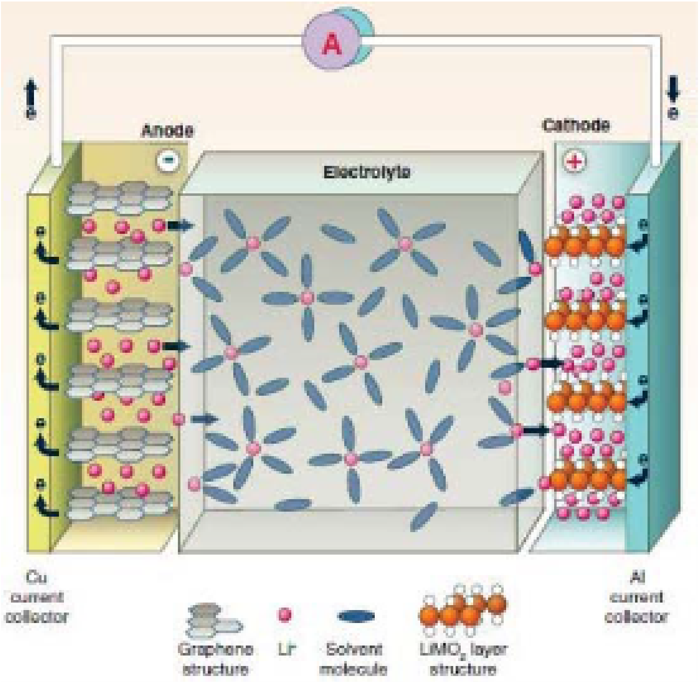

Figure 3.1: Projected cost decline of LIBs with EV production scale [5]

3.2 Operating Principle of Lithium-Ion Batteries

A typical lithium-ion battery consists of a graphite anode, a lithium metal oxide cathode, and an electrolyte containing lithium salt (such as $LiPF_6$) dissolved in a solvent like ethylene carbonate (EC) or dimethyl carbonate (DMC). During discharge, lithium ions move from the anode to the cathode through the electrolyte, while electrons travel through the external circuit to supply power to a load. The reverse occurs during charging, where lithium ions migrate back to the anode. The movement of lithium ions between electrodes enables energy storage and release. This intercalation-deintercalation mechanism allows for reversible cycling with high efficiency, which is a major advantage over older battery chemistries.

3.3 Classification of Lithium-Ion Battery Chemistries

Lithium-ion batteries are available in various chemistries, each offering distinct trade-offs between specific energy, cycle life, thermal stability, safety, and cost. The major chemistries include:

- Lithium Cobalt Oxide (LCO)
- Lithium Nickel Oxide (LNO)
- Lithium Nickel Cobalt Aluminium Oxide (NCA)
- Lithium Nickel Manganese Cobalt Oxide (NMC)
- Lithium Manganese Oxide (LMO)
- Lithium Iron Phosphate (LFP)
- Lithium Titanate Oxide (LTO)

Each of these chemistries is discussed in detail below.

3.3.1 Lithium Cobalt Oxide (LCO)

Lithium Cobalt Oxide ($LiCoO_2$) batteries are common in consumer electronics due to their high energy density and stable performance. Their layered structure allows efficient lithium-ion movement. However, high cost, limited cycle life, and poor thermal stability restrict their use in high-power or safety-critical applications like electric vehicles and grid storage. [7] [23] [24]

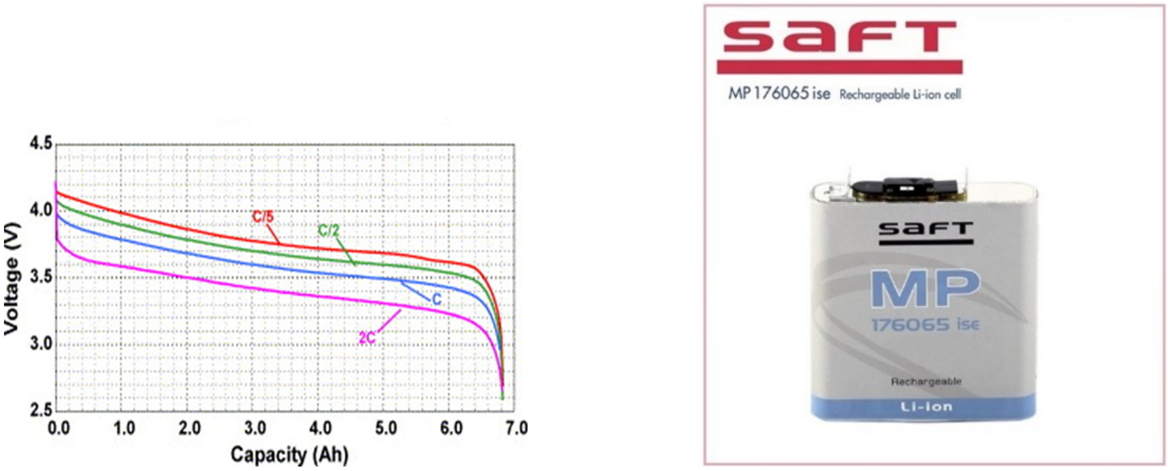

(a) Discharge characteristics at 20°C

(b) Prismatic battery cell

Figure 3.2: Saft MP 176065 LCO Prismatic Cell [6]

3.3.2 Lithium Nickel Oxide (LNO)

Lithium Nickel Oxide ($LiNiO_2$) has higher energy density and lower cobalt content than LCO, reducing costs. However, it faces thermal instability and structural degradation during cycling. Due to safety concerns and synthesis challenges, LNO is typically used as a doped base material to enhance performance and stability.

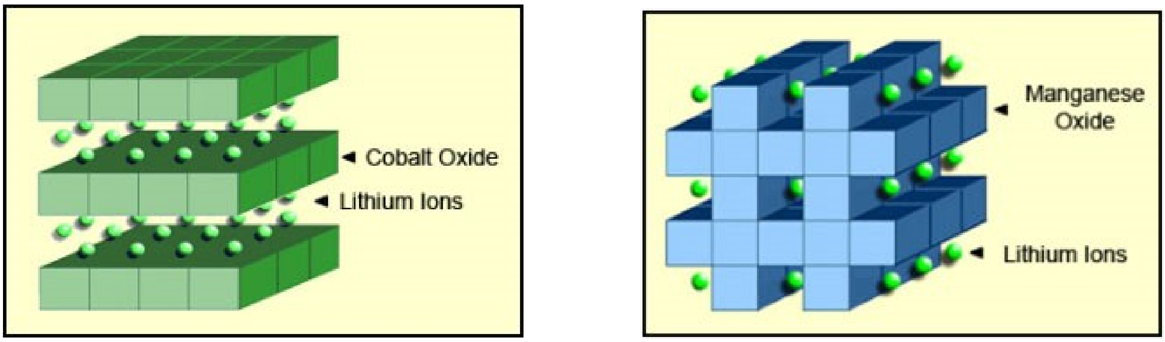

(a) LCO and LNO cathode structure

(b) LMO cathode structure

Figure 3.3: Layered vs spinel cathode structure [6]

(a) Panasonic NCR18650B cell (NCA) (b) Keeppower NCA battery cells

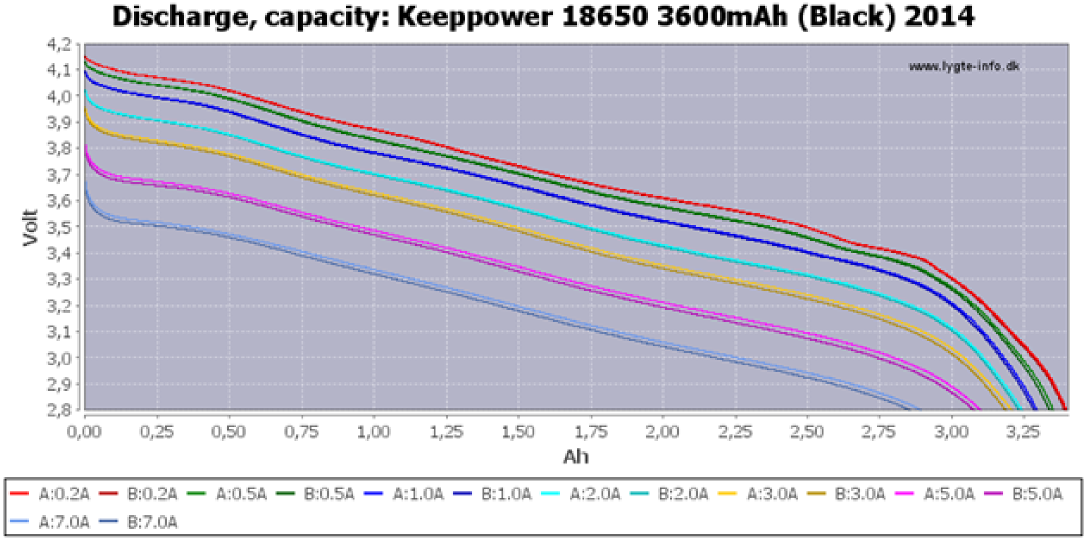

(c) Keeppwer 3600mA battery discharge characteristics

Figure 3.4: An example of an NCA battery [6]

3.3.3 Lithium Nickel Cobalt Aluminium Oxide (NCA)

Lithium Nickel Cobalt Aluminium Oxide ($LiNiCoAlO_2$) batteries offer high energy density, long cycle life, and improved thermal stability due to aluminium. Commonly used in electric vehicles, especially by Tesla, they provide high energy and power.

However, their high cost, complex management, and safety concerns require robust battery management systems. [7] [25]

3.3.4 Lithium Nickel Manganese Cobalt Oxide (NMC)

Lithium Nickel Manganese Cobalt Oxide ($LiNiMnCoO_2$) batteries balance energy density, power, cycle life, safety, and cost. Manganese improves thermal stability, while nickel and cobalt enhance capacity [26]. Widely used in EVs, power tools, and grid storage, variants like NMC 111, 532, and 811 optimize performance and cost, with higher nickel reducing cobalt dependency.

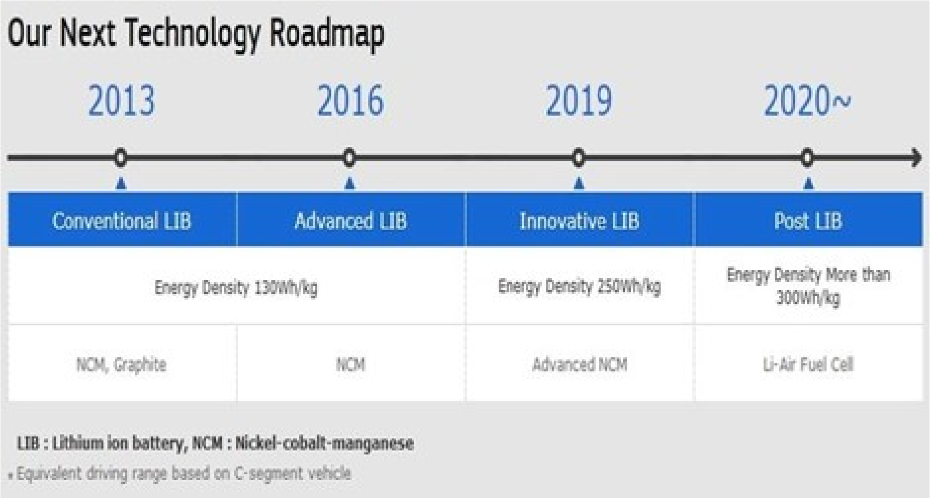

Our Next Technology Roadmap

2013	2016	2019	2020~
Conventional LIB	Advanced LIB	Innovative LIB	Post LIB
Energy Density 130Wh/kg		Energy Density 250Wh/kg	Energy Density More than 300Wh/kg
NCM, Graphite	NCM	Advanced NCM	Li-Air Fuel Cell

LIB : Lithium ion battery, NCM : Nickel-cobalt-manganese

• Equivalent driving range based on C-segment vehicle

Figure 3.5: Samsung SDI - Battery technology roadmap [5]

3.3.5 Lithium Manganese Oxide (LMO)

Lithium Manganese Oxide ($LiMn_2O_4$) batteries feature a spinel structure allowing 3D lithium diffusion, delivering high power and good thermal stability. Commonly used in power tools, e-bikes, and hybrids, LMO offers safety and low cost but has lower energy density and shorter cycle life, especially at high temperatures. [4]

3.3.6 Lithium Iron Phosphate (LFP)

Lithium Iron Phosphate ($LiFePO_4$) batteries are valued for their excellent thermal and chemical stability, long cycle life, and high safety. The olivine structure provides strong P–O bonds, minimizing oxygen release and reducing thermal runaway risk. Despite a lower nominal voltage (about 3.2 V) and energy density compared to NCA or NMC, LFP is preferred for stationary storage, electric buses, and commercial vehicles due to its cost-effectiveness and reliability. [7]

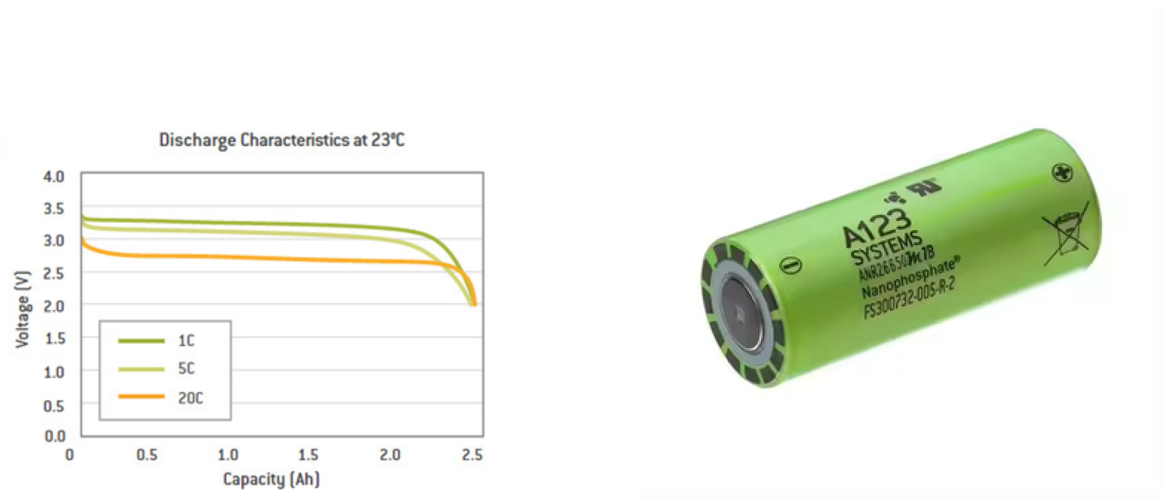

(a) Discharge characteristics at T = 23°C (b) A123 battery cell

Figure 3.6: LFP battery - ANR26650m1-B series by A123 Systems [6]

3.3.7 Lithium Titanate Oxide (LTO)

Lithium Titanate ($Li_4Ti_5O_{12}$) replaces the traditional graphite anode with a lithium titanate structure, enabling fast charging, long cycle life, and high safety. LTO cells show minimal volume change and strong thermal stability. However, they have a lower nominal voltage (around 2.4 V) and reduced energy density, leading to larger size and higher cost. LTO is increasingly used in rapid charging and long-life applications like public transport and telecom backup power. [7]

3.4 Comparative Evaluation of LIB Chemistries

The choice of lithium-ion battery chemistry is heavily dependent on the application. NCA and NMC provide high specific energy and long cycle life, making them ideal for electric mobility. LFP, while offering lower energy density, provides unmatched thermal stability, safety, and cost advantages, which make it highly suitable for grid energy storage systems (GESS). LTO, though expensive and bulky, is superior in safety and longevity. A comparative evaluation of all chemistries reveals that no single battery type is optimal for all parameters, and trade-offs must be made depending on whether the application prioritizes energy density, power, cost, safety, or lifecycle.

3.5 Comparison of Current Lithium-Ion Battery (LIB) Chemistries

This sub-section provides a comparative overview of the main performance parameters of commercially available LIB chemistries. Table 3.1 summarizes the key metrics such as specific capacity, nominal voltage, specific energy, cycle life, safety, lifetime, and cost.

Table 3.1: Comparison of various LIB chemistries [7]

Type	**Specific Capacity (mAh/g)**	**Nominal Voltage (V)**	**Specific Energy (Wh/kg)**	**Cycle Life**	**Safety**	**Lifetime**	**Cost**
LCO	140	3.7	110–190	500–1000	Poor	Average	High
LMO	146	3.8	100–120	1000	Average	Poor	Average
NCA	180	3.6	100–150	2000–3000	Low	High	High
NMC	145	3.6	100–170	2000–3000	Low	Good	High
LFP	170	3.3	90–115	>3000	High	Average	Average
LTO	170	2.2	60–75	>5000	High	High	High

A graphical representation of these chemistries' performance parameters is shown in Figure 3.7.

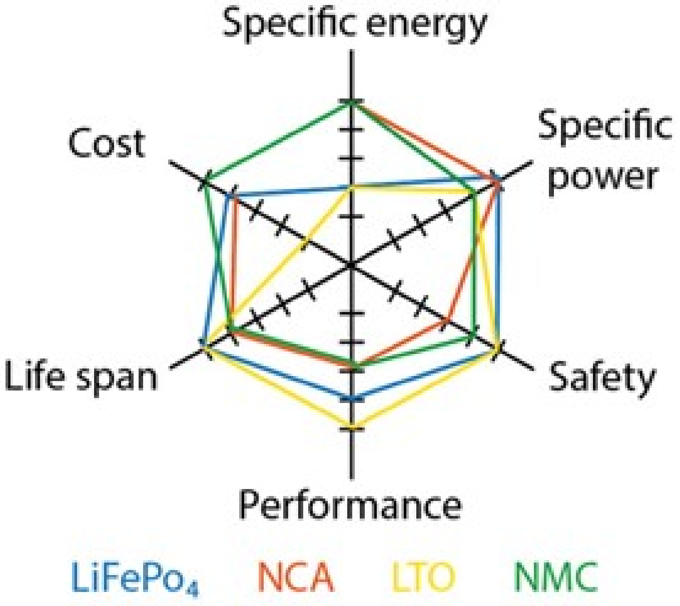

Figure 3.7: Comparison of various Li-ion chemistries [7]

Conclusion: From a grid energy storage system (GESS) perspective, NCA and NMC offer the best specific energy and reasonable cycle life but suffer from low safety and high cost. LMO and LFP offer better safety and cost profiles, though LMO's limited cycle life restricts its application. For stationary applications where specific energy is less critical, LFP emerges as the most balanced option due to its safety, lifetime, power capability, and reasonable cost. If LTO's cost reduces, it could become a strong candidate for GESS applications because of its high safety, rapid charge/discharge capability, and very long cycle life. It is essential to monitor ongoing developments in these technologies, particularly regarding cost and performance improvements. Emerging lithium-based battery technologies discussed in the following section warrant careful observation for their potential future impact.

3.6 Advanced Lithium-Based Battery Technologies

3.6.1 Lithium-Air Batteries

Lithium-air batteries offer very high theoretical energy density (up to 3500 Wh/kg) by using a lithium metal anode and an air cathode. Despite this potential, challenges like low efficiency, poor cycle life, and sensitive packaging keep them in early research stages. [7]

3.6.2 Lithium-Sulphur Batteries

Lithium-sulphur batteries provide high specific energy (up to 500 Wh/kg) and low cost using a lithium anode and sulphur cathode. Their commercialization is hindered by capacity loss due to the polysulfide shuttle effect, though ongoing research aims to address these issues. [7]

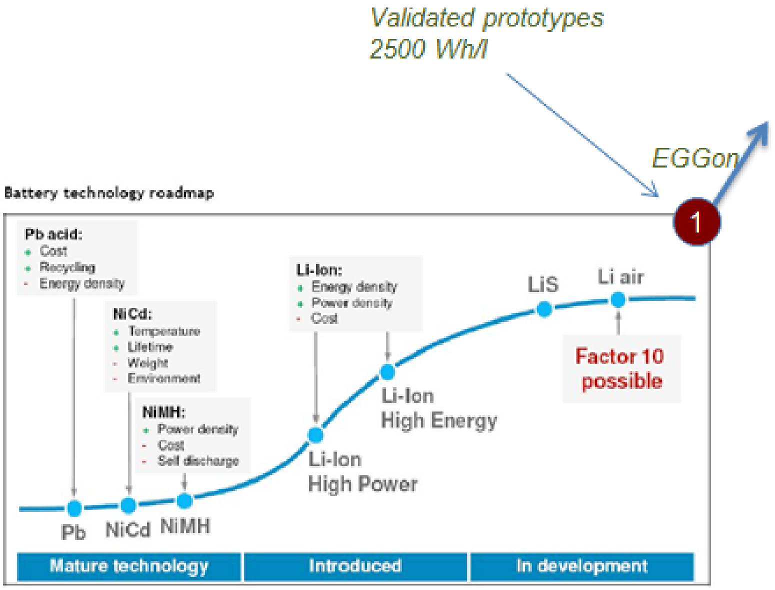

Figure 3.8: An outlook for development of LIBs, where factor 10 means that the future LIBs should reach 10x the energy density of the current LIBs. [8]

3.7 Summary and Relevance to Grid Energy Storage

In conclusion, lithium-ion batteries have undergone extensive development and diversification. Each chemistry offers unique advantages and challenges. Among all commercially available chemistries, Lithium Iron Phosphate (LFP) is particularly suitable for grid energy storage systems due to its inherent safety, thermal stability, long lifespan, and cost efficiency. [8] For electric vehicle applications, high energy density chemistries like NMC and NCA are preferred, while Lithium Titanate (LTO) can be utilized in fast-charging, long-life applications if cost barriers are addressed. Looking ahead, lithium-air and lithium-sulphur batteries may revolutionize the energy storage landscape if their current limitations can be overcome through innovative material science and engineering. [8]

Chapter 4

Battery Phenomena and Management

4.1 Battery Phenomena

Although a battery may seem like a generally simple device that allows it to store and release electric energy, in its essence, it is a rather complicated unit that requires considerable attention. The main complexity of the battery comes from its internal chemistry and structure that affect its external character and performance, as also portrayed in Chapter 3. In this section, it is intended to elaborate on some of the main characteristics of a LIB as a background for the forthcoming chapters that will be devoted to LIB modeling.

4.1.1 Rate-dependent Capacity (C-rate Effect)

The C-rate effect describes the decrease in usable battery capacity at high charge or discharge rates. This occurs because, at high currents, ion diffusion in the electrolyte lags behind the electrochemical reactions, leading to incomplete utilization of active materials [27] [28]. Charging or discharging at lower rates allows more complete reactions, recovering capacity. This behavior is illustrated in (Fig. 4.3).

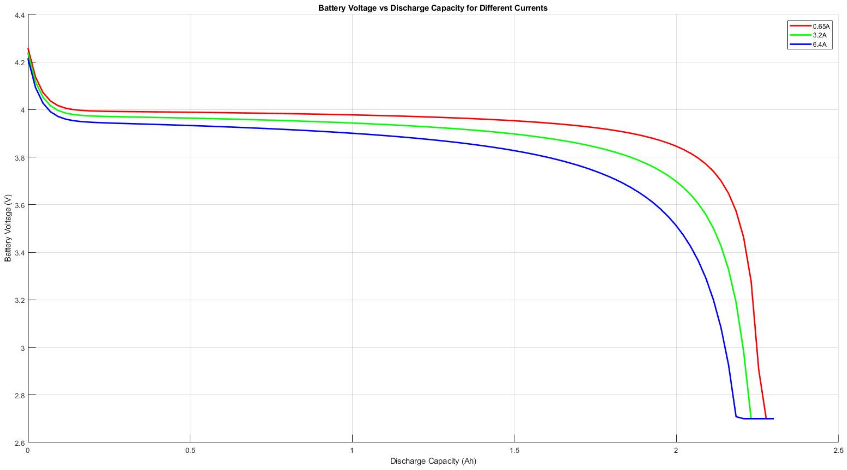

Figure 4.1: Effect of C-rate on battery capacity. [9]

4.1.2 Temperature Effect

Temperature significantly influences battery performance. Lithium-ion batteries operate optimally within the range of 23–25 textdegree C. At lower temperatures, internal resistance increases and chemical activity slows down, reducing performance. Conversely, higher temperatures reduce resistance and can temporarily increase capacity, but they also elevate the self-discharge rate due to increased internal chemical reactions [27] [29] [28].

4.1.3 Self-discharge

Self-discharge denotes the spontaneous loss of charge in a battery without any external load. Although all battery chemistries experience self-discharge, lithium-ion batteries exhibit relatively low self-discharge rates, as summarized in Table 4.1. It is also temperature and SOC dependent; higher temperatures and higher SOCs tend to accelerate self-discharge [30] [29].

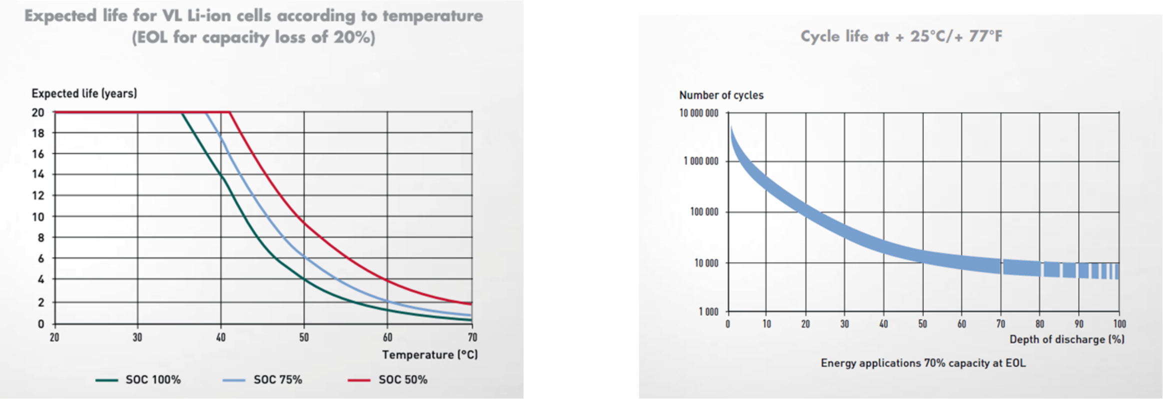

(a) (b)

Figure 4.2: LIB characteristics a) Calendar life vs temperature and SOC, b) Cycle life vs DOD. [9]

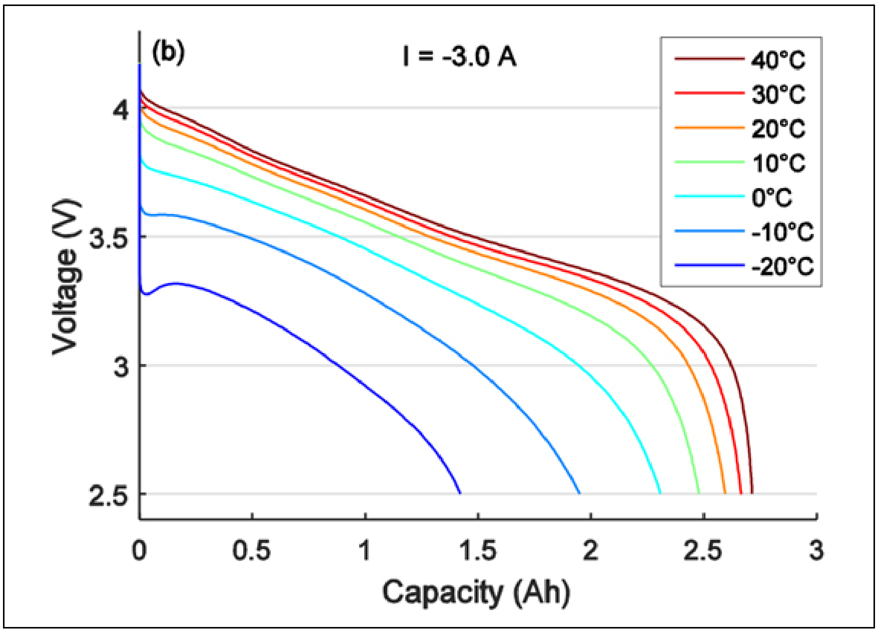

Figure 4.3: Effect of battery capacity due to Temperature. [9]

Table 4.1: Self-discharge rates of common battery chemistries

Battery Type	**Self-discharge Rate (per month)**
Nickel-Cadmium (NiCd)	15–20%
Nickel-Metal Hydride (NiMH)	20–30%
Lithium-Ion (Li-ion)	2–3%
Lead-Acid	4–6%

4.1.4 Aging Effect (Capacity Fade)

Capacity fade, or battery aging, is the irreversible decline in battery capacity over time due to repeated charge-discharge cycles. It directly impacts the battery's cycle life. High C-rates, overcharging, and deep discharges (high Depth of Discharge or DOD) accelerate this phenomenon. Fig. 4.4a depicts the impact of DOD on cycle life. Physically, aging results from processes like electrolyte decomposition, formation of passive films, and dissolution of active materials. These increase internal resistance and can lead to battery failure. Mitigation strategies include operating the battery at lower C-rates, limiting DOD, and charging to a reduced cut-off voltage [31], [27]. Fig. 4.4a and Fig. 4.4b compare macrocycle and combined cycle approaches, highlighting their influence on battery life.

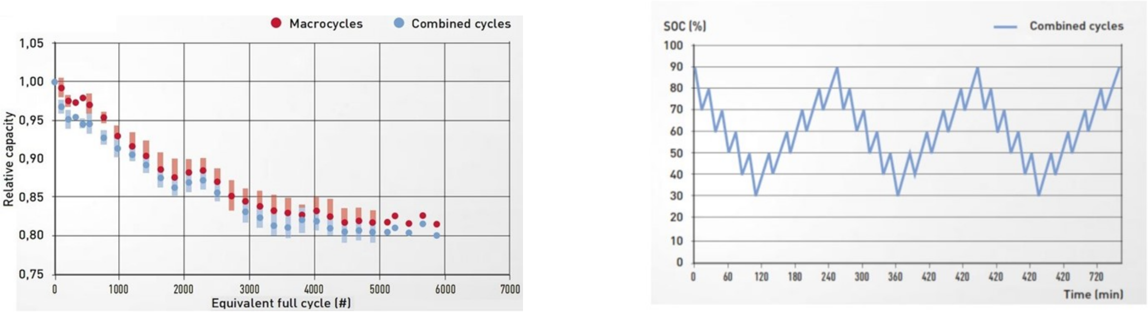

(a)

(b)

Figure 4.4: LIB characteristics a) Macrocycle/Combined cycle vs Cycle-life, b) Combined cycle example. [9]

4.2 Battery SOC and SOH

Battery SOC (State of Charge)

SOC represents the remaining charge or usable energy in a battery. Since it cannot be measured directly, estimation techniques are employed. Table 4.2 classifies these methods into four categories:

1. Direct Measurement (e.g., Open Circuit Voltage, Terminal Voltage, Impedance methods) – Generally less accurate and often unsuitable for real-time applications.

2. Book-keeping Estimation (e.g., Coulomb Counting, Modified Coulomb Counting) – Commonly used due to their simplicity and moderate accuracy.

3. Adaptive Systems (e.g., Kalman Filter variants, Neural Networks) – Provide high accuracy and can adapt to dynamic conditions.

4. Hybrid Methods (e.g., Coulomb Counting + Kalman Filter) – Combine multiple techniques for improved accuracy.

Among these, adaptive systems like the Kalman Filter (including EKF and UKF) and Lyapunov-Based methods show promising accuracy, provided detailed battery data is available [32].

Table 4.2: Classification of SOC estimation methods

Category	**Examples**
Direct Measurement	OCV, Terminal Voltage, Impedance
Book-keeping Estimation	Coulomb Counting, Modified Coulomb Counting
Adaptive Systems	Kalman Filters (EKF, UKF), Neural Networks
Hybrid Methods	Coulomb Counting + Kalman Filter

Battery SOH (State of Health)

SOH assesses the current condition of a battery relative to its original state. Like SOC, it is not directly measurable and must be estimated. Capacity fade trends are typically used to infer SOH. Advanced SOC estimation techniques, such as Kalman Filters and Lyapunov-Based methods, have been extended to estimate SOH as well [13] [33]. Although SOH is less critical for day-to-day operation, it is vital for long-term performance and safety assessment.

4.3 Li-ion Battery Pack Concept

A typical lithium-ion battery pack comprises numerous individual cells arranged in series-parallel configurations to form modules. Several modules combine to form a tray, each managed by a dedicated Battery Management System (BMS) to ensure safe operation and uniform charging/discharging [34]. Fig. 4.5 shows an example of a battery tray from Panasonic containing 312 18650-type cells.

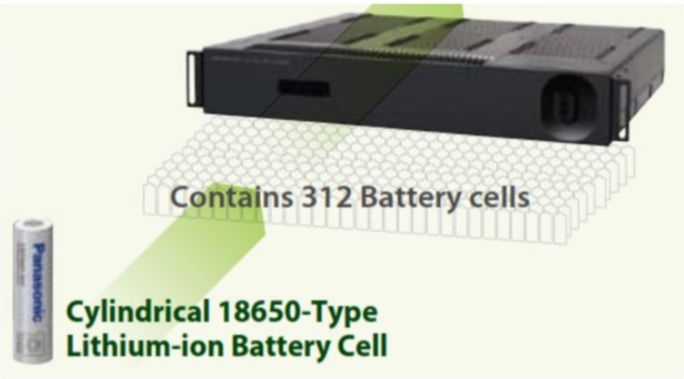

Figure 4.5: LIB tray - Panasonic. [10]

Multiple trays form a battery rack, which typically delivers voltages between 500-1000 V. A main BMS oversees the entire rack, communicates with the Power Conditioning System (PCS), and reports key parameters like terminal voltage, SOC, and

SOH. Fig. 4.6 illustrates a battery pack from LG Chem, showing the full assembly from individual prismatic cells to container-scale storage solutions.

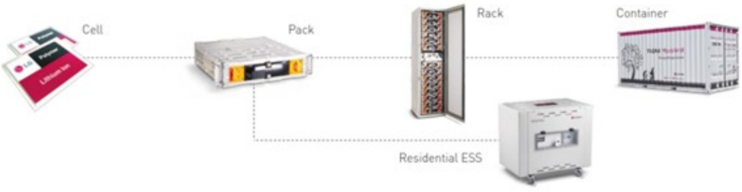

Figure 4.6: LIB Assembly for a GESS by LG Chem. [11]

For high-energy applications, multiple racks can be paralleled with corresponding PCSs, forming containerized storage systems with capacities in the MW/MWh range. Detailed information about such configurations is provided in Appendix E and F, including examples from Saft and NEC Energy Systems, respectively. In particular, the NEC racks use A123 Systems LFP battery cells, known for their safety and stability [35].

Chapter 5

Battery Modeling – Literature Review

The growing interest in batteries and energy storage systems, initially driven by battery-powered consumer electronics such as mobile phones and laptops, has recently expanded significantly due to advancements in electric vehicles (EVs) and grid energy storage applications. Consequently, a wide range of battery models have been developed and reported in the literature.

These models are generally categorized into four main groups: physical models, empirical models, abstract models, and hybrid models that combine elements from the previous three categories [27] [28].

5.1 Physical Models

Physical models represent the battery based on its fundamental electrochemical processes and internal chemistry. These models tend to be highly detailed and complex, requiring numerous input parameters and comprehensive knowledge of the battery's chemical composition. As a result, physical models demand substantial computational resources but provide very high accuracy. This makes them particularly suitable for battery cell development and research laboratories.

However, for practical applications such as battery emulator systems, the complexity and computational demands of physical models often become prohibitive, especially when deployed on resource-constrained hardware [27] [28] [36].

Among physical models, single particle models (SPM) and pseudo-double dimension (P2-D) models are widely recognized for lithium-ion batteries (LIB) [36]. Fig. 5.1 illustrates the general relationship between model complexity (computational power) and accuracy, showing an increasing trend in computational requirements with higher model fidelity.

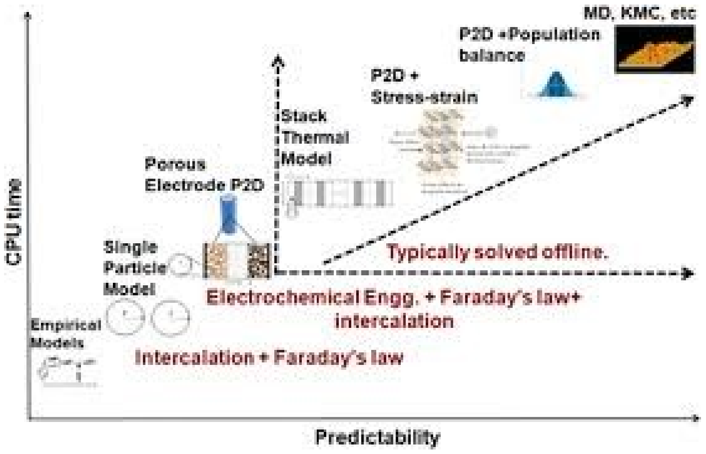

Figure 5.1: Physical battery models - computational power vs model's accuracy [5]

To mitigate computational burdens, reduced-order physical models have been developed that simplify full physical models while retaining an acceptable level of accuracy, depending on the degree of simplification [28].

5.2 Empirical Models

Empirical models differ significantly from physical models in that they are typically simple and require minimal computational power. These models generally rely on fitting mathematical functions to experimentally obtained charge and discharge curves. Common mathematical functions used include trigonometric, logarithmic, polynomial, exponential, and power-law functions [36].

A notable example is the Shepherd's original model, alongside variants such as the Unnewehr Universal Model and the Nernst Model. These three models, expressed in their generic forms, are:

$$V = V_0 - Ri - \mu/\mathrm{SOC} \tag{5.1}$$

$$V = V_0 - Ri - \mu(\mathrm{SOC}) \tag{5.2}$$

$$V = V_0 - Ri + \mu_1 \ln(\mathrm{SOC}) + \mu_2 \ln(1 - \mathrm{SOC}) \tag{5.3}$$

Where V is the terminal voltage, V_0 is the nominal voltage, R is the internal resistance, i is the current (positive for discharge, negative for charge), and μ, μ_1, μ_2 are fitting parameters. These models vary in accuracy depending on the application. Shepherd's model performs well in predicting terminal voltage during continuous current discharge, whereas the Nernst model better handles dynamically varying currents. The Universal model provides the most accurate State of Charge (SOC) estimate among the three [36].

Shepherd's original model, developed in 1963 [37], remains popular due to its simplicity and minimal parameter requirements derived from manufacturer datasheets. A modified version of this model, which includes separate equations for charge and discharge modes, offers improved accuracy and has found use in simple EV battery

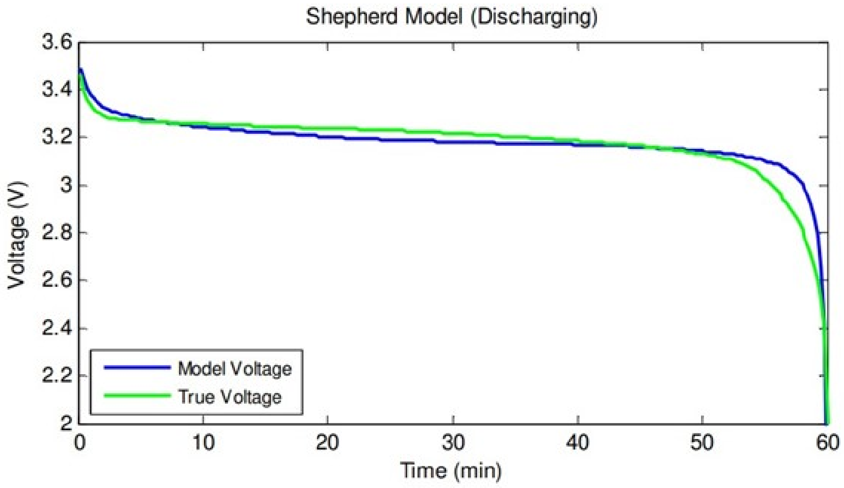

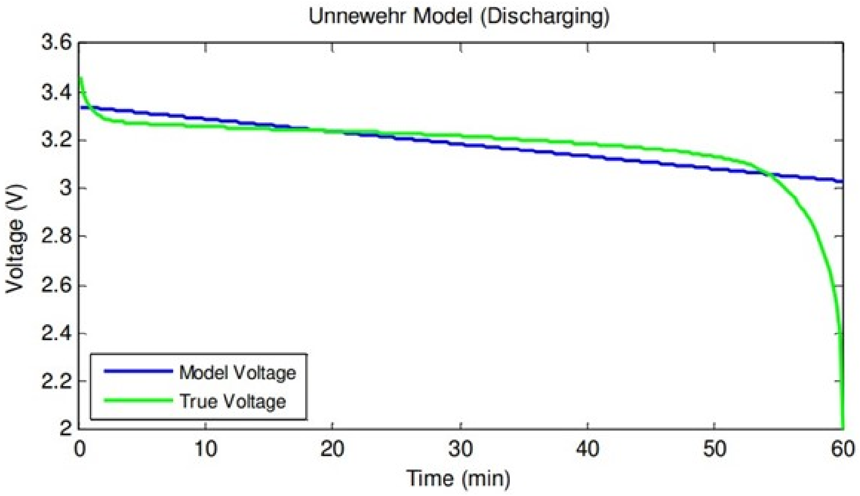

modeling, as well as MATLAB-Simulink and PSIM implementations [38], [39], [40], [41], [42].

Despite their simplicity and low computational cost, empirical models suffer from limited accuracy when more detailed battery behavior is required. Other empirical approaches, such as Peukert's law, battery efficiency models, and Weibull fit models, have been proposed to enhance predictive capability but have not shown significant overall improvements [27].

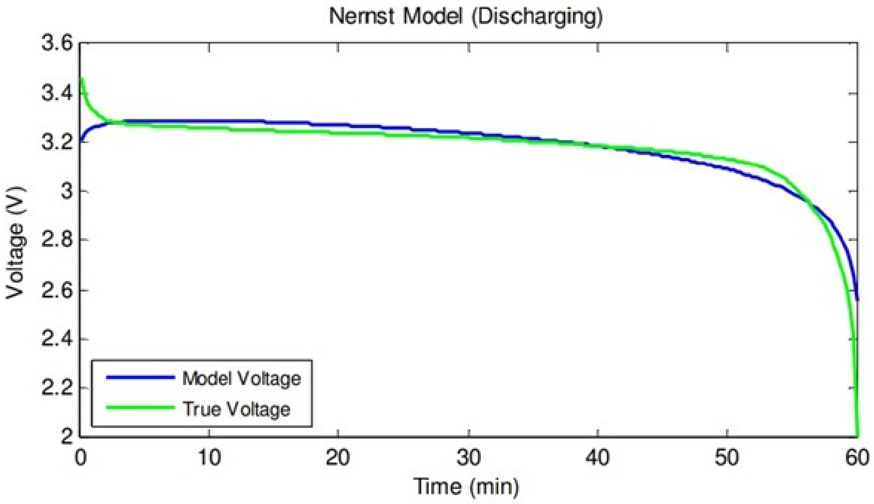

Figure 5.2: Comparison of three different empirical models in a continuous discharging mode [12]

5.3 Abstract Models (Equivalent Electrical Circuit Models - EECMs)

Abstract models, often referred to as Equivalent Electrical Circuit Models (EECMs), represent battery behavior using electrical components such as resistors, capacitors, and diodes to mimic the battery's external electrical characteristics. These models strike a balance between computational complexity and accuracy, often outperforming empirical models in terms of prediction fidelity [27].

EECMs require physical access to the actual battery for parameter identification, which typically involves extensive testing [28] [43] [44] [45] [13].

There are three common types of EECMs:

- **Impedance-based EECM:** Uses Electrochemical Impedance Spectroscopy (EIS) to measure the battery's impedance at various frequencies by applying small AC signals. While this method can characterize battery impedance accurately, it requires offline testing with specialized equipment and does not support real-time parameter updates [28]. Figure 5.3a illustrates such a model.

- **Voltage-Current (V-I) based EECM:** Utilizes measurements of battery current and open-circuit voltage (OCV) to derive the model. The typical structure includes a controlled voltage source representing OCV, an internal series resistance, and one or more RC networks to capture dynamic behavior. The Thevenin model (1st order EECM) and Dual Polarization (DP) model (2nd order) are common examples, with higher-order models used as a trade-off between complexity and accuracy [18], [28], [46], [44]. Figure 5.3b shows the Thevenin model with series and transient RC elements.
- **Run-time based EECM:** Models battery runtime characteristics such as C-rate effects and provides reasonable accuracy during continuous charge/discharge, but struggles with dynamic load conditions due to increased complexity [47], [44].

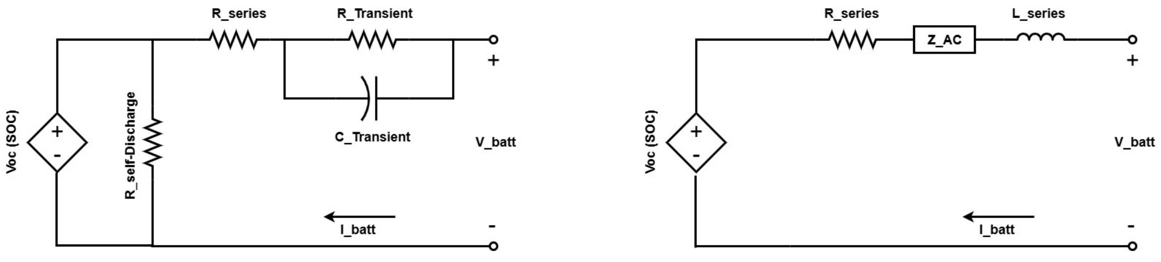

(a) Thevenin (RC) model

(b) Impedance model

Figure 5.3: EECM

State-of-the-art EECMs combine elements from Thevenin and Run-time models to achieve accurate voltage and SOC estimation under both static and dynamic conditions while including runtime effects [47] [44] [34]. Figure 5.4 illustrates such an advanced EECM, where a SOC-dependent controlled current source charges a capacitor representing SOC, with temperature and degradation factors sometimes included.

The dual RC model accounts for dynamic relaxation phenomena, while the lookup table relates SOC to OCV.

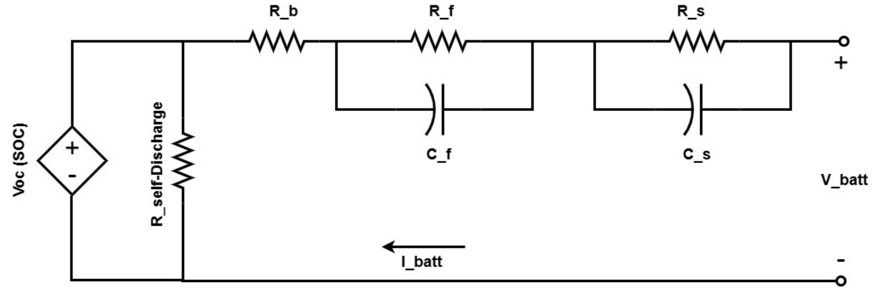

Figure 5.4: Graphical representation of the advanced EECM [13]

Overall, EECMs offer a compelling balance of accuracy and computational efficiency, with sophisticated parameter estimation techniques enabling SOC, terminal voltage, and State of Health (SOH) estimations, making them suitable for Battery Management Systems (BMS). Their main limitation lies in the complexity of parameter identification, requiring rigorous testing [45] [43] [13] [12] [48] [49].

5.4 Other Models

Several alternative modeling approaches have also been explored:

- **Bio-inspired black-box models:** These use intelligent algorithms, such as artificial neural networks or wavelet neural networks, to model battery behavior. While these models can achieve reasonable accuracy, they demand high computational resources and extensive training data. They also require significant prior knowledge about the battery [28].
- **Other approaches:** Models such as stochastic models, transmission line models, and hydrodynamic models focus on specific battery characteristics but can-

not generally comprehensively represent full battery behavior, resulting in limited adoption [28].

5.5 Operating Principle, Battery Modeling, and Case Study

5.5.1 Functional Overview of the Model-Based Emulator

The lithium-ion battery emulator developed in this project operates using a model-based closed-loop control architecture. This system is structured into three primary stages: **modeling**, **actuation**, and **sensing**.

- **Modeling Stage:**

  In this stage, a dynamic lithium-ion battery model implemented in software calculates the reference terminal voltage $V_{\text{batt,ref}}$. This value is determined based on the present and historical values of the battery current I_{batt}. The reference voltage serves as the desired output for the hardware to emulate.

- **Actuation Stage:**

  A switching-mode power converter generates a physical voltage that tracks the computed $V_{\text{batt,ref}}$, simulating the electrical response of a real battery. This voltage output can be connected to external loads, both active and passive.

- **Sensing Stage:**

  The actual current I_{batt} drawn by or supplied to the load is measured and fed back to the model. This feedback mechanism ensures dynamic adjustment of the reference voltage, thereby enabling realistic emulation of battery behavior.

The emulator's accuracy depends on several factors, including the fidelity of the battery model, converter bandwidth, switching ripple, and passive component tolerances. Despite these limitations, such discrepancies are typically negligible in energy-oriented applications such as Battery Energy Storage Systems (BESS), especially when well-designed inductors and capacitors are employed to minimize voltage ripple and enhance transient response.

The MATLAB/Simulink-based closed-loop control structure implemented for the battery emulator is shown in Figure 5.5.

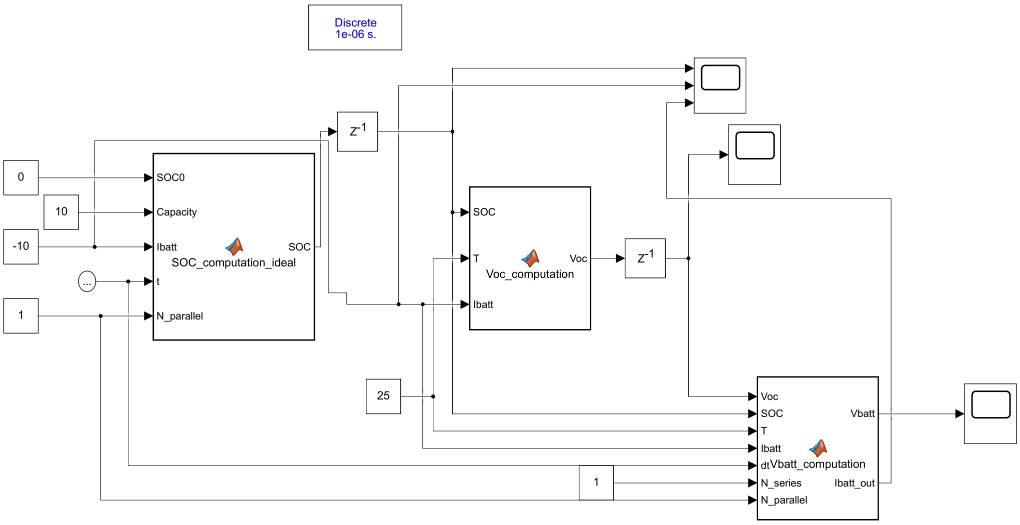

Figure 5.5: MATLAB Simulink model of the model-based lithium-ion battery emulator.

5.5.2 Selection and Description of the Battery Model

Numerous battery modeling techniques are found in the literature, including electrochemical, stochastic, analytical, and equivalent circuit-based methods. Among these, the equivalent circuit approach is particularly attractive due to its balance between accuracy and computational simplicity.

In this project, a hybrid dynamic equivalent circuit model was chosen, which combines electrical elements with a nonlinear voltage-SOC (State of Charge) relationship. This model includes:

- A series resistance R_i representing the internal resistance.
- An RC pair R_t, C_t modeling transient response to load variations.
- An open circuit voltage V_{OC} calculated from SOC using a polynomial + exponential function.

The state of charge and corresponding open-circuit voltage are defined as:

$$SOC = SOC_0 - \frac{1}{3600Q} \int I_{\text{batt}}\, dt \tag{5.4}$$

$$V_{OC} = a_3 SOC^3 + a_2 SOC^2 + a_1 SOC + a_0 + a_5 e^{a_4 \cdot SOC} \tag{5.5}$$

Where:

- Q is the nominal battery capacity in Ah.
- SOC_0 is the initial state of charge.
- a_0 to a_5 are model coefficients obtained from experimental data.

This model is computationally efficient, has a small parameter set, and has been validated in previous studies with high precision (average error 42%).

Although this model does not account for thermal dynamics or aging, these aspects can be incorporated. Extended versions of the model can include power loss, temperature effects, and state-of-health (SOH) degradation. Such enhancements would rely on external environmental inputs and additional parameter identification, without altering the emulator's fundamental design.

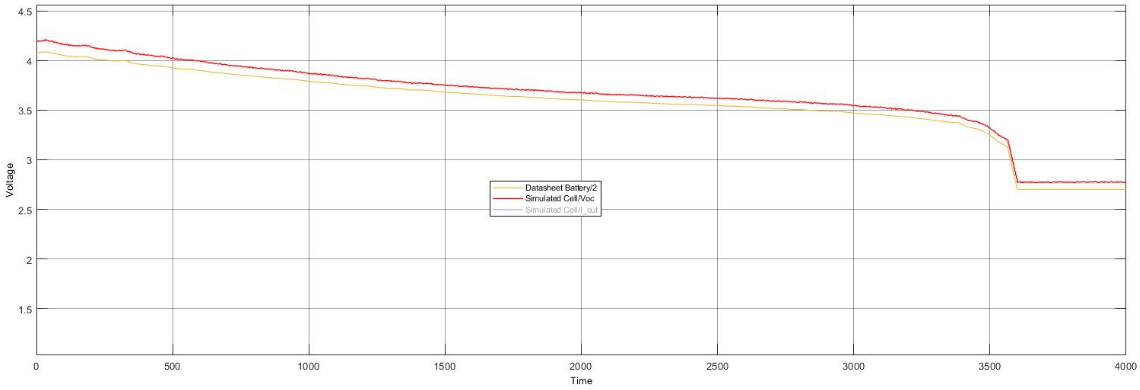

Figure 5.6: Comparison of real and simulated battery terminal voltage using the developed model.

To validate the accuracy of the hybrid equivalent circuit model, simulations were conducted under various load conditions. The simulated voltage profile was found to closely follow the real voltage profile obtained from experimental data, indicating strong agreement.

5.5.3 Case Study: Kokam Li-ion Polymer Cell

To test and validate the emulator, a case study was conducted using a high-performance commercial lithium-ion polymer cell—Kokam SLBP55205130H.

This pouch-type cell uses Nickel Manganese Cobalt (NMC) chemistry, known for its high-power density, long cycle life, and thermal stability.

A battery pack was assembled using 30 of these cells connected in series. The technical specifications are summarized below:

Table 5.1: Technical Specifications of Kokam Cell Pack

Parameter	**Single Cell**	**30-Cell Pack**
Nominal Voltage	3.7 V	111 V
Capacity	11 Ah (40.7 Wh)	11 Ah (1221 Wh)
Charge Limit Voltage	4.3 V	129 V
Discharge Limit Voltage	2.7 V	81 V
Weight	0.28 kg	∼9 kg
Dimensions (mm)	207×137×5.6	∼240×170×180

This pack configuration serves as the reference system for emulator design. Nevertheless, the same emulator framework can be used to mimic different battery technologies by updating the corresponding model and parameters.

5.5.4 Parameter Identification Strategy

To implement the battery model, nine parameters must be determined:

- Three electrical elements: R_i, R_t, C_t
- Six coefficients: a_0 to a_5 defining the VOC-SOC relationship

Electrical Parameter Extraction:

1. Charge the battery to full capacity.

2. Discharge at a constant current and record the terminal voltage until it reaches its minimum.

3. Measure the internal resistance during load connection:

$$R_i = \frac{V_0 - V_1}{I} \tag{5.6}$$

4. After load disconnection, observe the voltage relaxation:

$$R_t = \frac{V_{oc} - V_t'}{I} \tag{5.7}$$

$$C_t = \frac{\tau}{R_t} \tag{5.8}$$

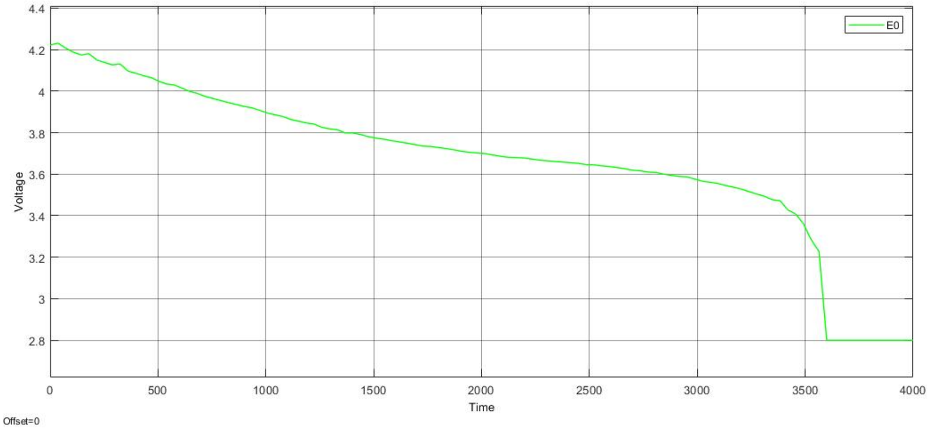

Figure 5.7: Extracted E0 (Open Circuit Voltage) lookup table from experimental data.

The E0 curve was obtained by applying small discharge pulses at steady-state intervals and plotting the resulting stabilized voltage. This data was curve-fitted using polynomial and exponential segments for high accuracy in modeling the nonlinear characteristics of the battery.

VOC-SOC Curve Fitting:

- Apply small discharge pulses (∼1% capacity) and allow voltage to stabilize.
- In the 20–100% SOC range, fit a cubic polynomial:

1. Fit the polynomial to the OCV-SOC curve:

$$p(SOC) = a_3 SOC^3 + a_2 SOC^2 + a_1 SOC + a_0 \tag{5.9}$$

2. In the 0–10% range, fit the exponential tail:

$$\log(V_{OC} - p(SOC)) = a_4 SOC + \log(a_5) \tag{5.10}$$

The final set of parameters used in the emulator is listed below:

Table 5.2: Final Parameters for Emulator Implementation

Parameter	**Single Cell**	**30-Cell Pack**
R_i (Internal Resistance)	3.3 mΩ	99 mΩ
R_t (Transient Resistance)	15 mΩ	450 mΩ
C_t (Capacitance)	555 F	18.5 F
$a_3,\ a_2,\ a_1,\ a_0$	0.315, 0.075, 0.495, 3.575	9.45, 2.25, 14.85, 107.25
$a_5,\ a_4$	1.035, 35	31.05, 35

Experimental validation showed that the reconstructed V_{OC}-SOC curve closely aligned with real battery behavior, confirming the effectiveness of the modeling and identification process.

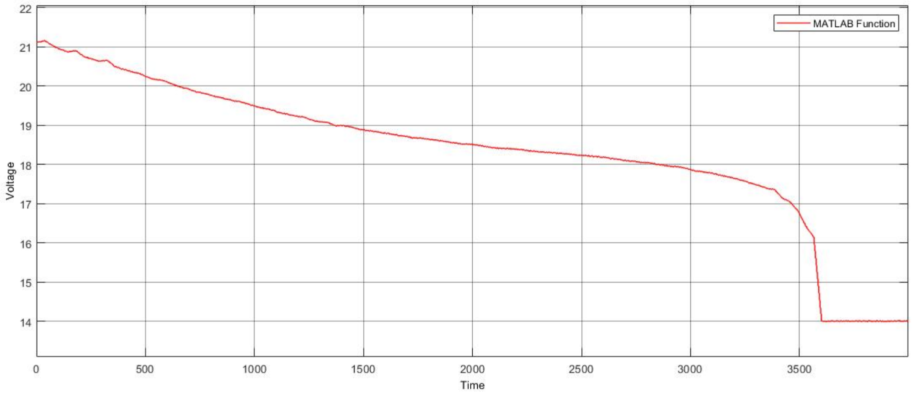

Figure 5.8: Simulated battery voltage (Vbatt) profile during discharge cycles.

The voltage response across different SOC levels confirmed the emulator's fidelity in replicating the transient and steady-state behavior of the real battery pack, especially during dynamic load conditions. Fig.5.9a and Fig.5.9b show the voltage vs. time characteristics during the charging process for a single cell and a multi-cell configuration, respectively. Fig.5.9a illustrates the typical CC-CV charging profile of a single Li-ion cell. The voltage rises steadily during the constant current phase and stabilizes during the constant voltage phase as the charging current tapers off. Fig.5.9b presents the voltage response of a multi-cell series pack. The overall profile follows a similar CC-CV pattern, but the total voltage increases more rapidly due to the series connection. Minor variations in the voltage slope may occur due to inter-cell imbalance.

These plots demonstrate the scalability of the charging behavior from single to multiple cells and support the accuracy of the modeled charging dynamics.

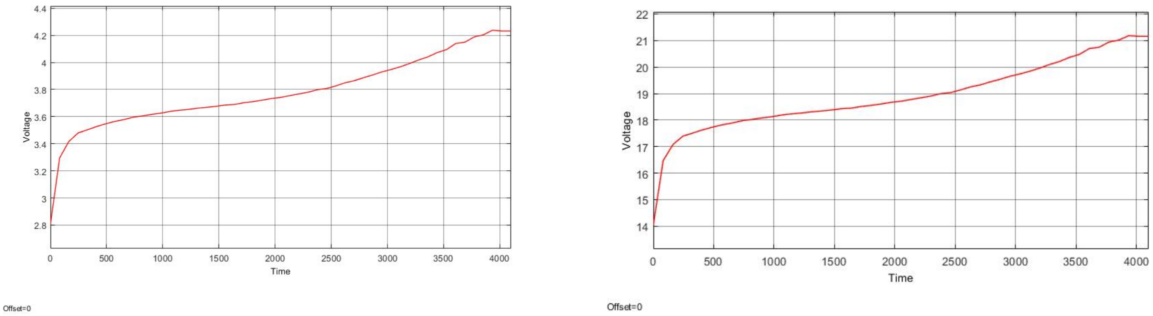

(a) Voltage vs Time during charging

(b) CC Charging

Figure 5.9: Charging behavior plots: (a) Single Cell, (b) Multiple Cell

The graphs depicting State of Charge (SOC), charging current, and cumulative capacity (Ah) provide insight into the battery's dynamic behavior during the charging process. The SOC curve shows the gradual increase in battery charge level over time, corresponding with the controlled charging current profile. The current graph illustrates the transition from constant current to constant voltage mode, where the current decreases as the battery approaches full charge. The Ah graph represents the total charge delivered to the battery, confirming the capacity utilization during the charging cycle.

Together, these plots validate the consistency between the charging current, SOC progression, and capacity gain, supporting the accuracy of the battery model under test conditions.

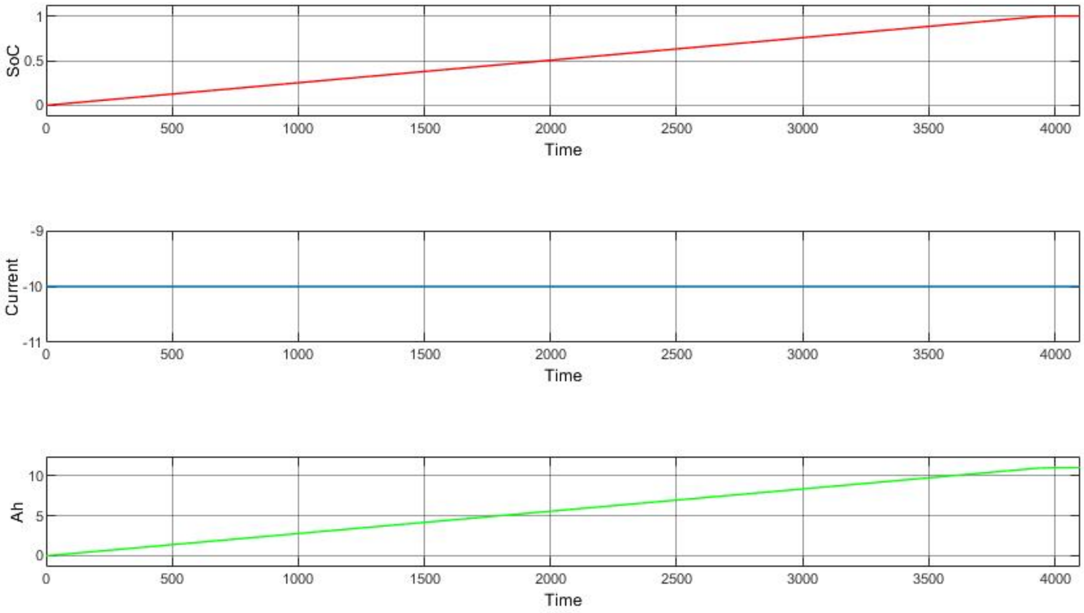

Figure 5.10: State of Charge (SOC), charging current, and cumulative capacity (Ah) profiles during the battery charging process.

The SOC versus voltage graph illustrates the relationship between the battery's state of charge and its terminal voltage during the charging/discharging cycle. This characteristic curve reflects the battery's electrochemical behavior, showing a nonlinear voltage increase with SOC, especially in the mid-range, followed by a plateau near full charge. This plot is essential for SOC estimation and battery management system calibration.

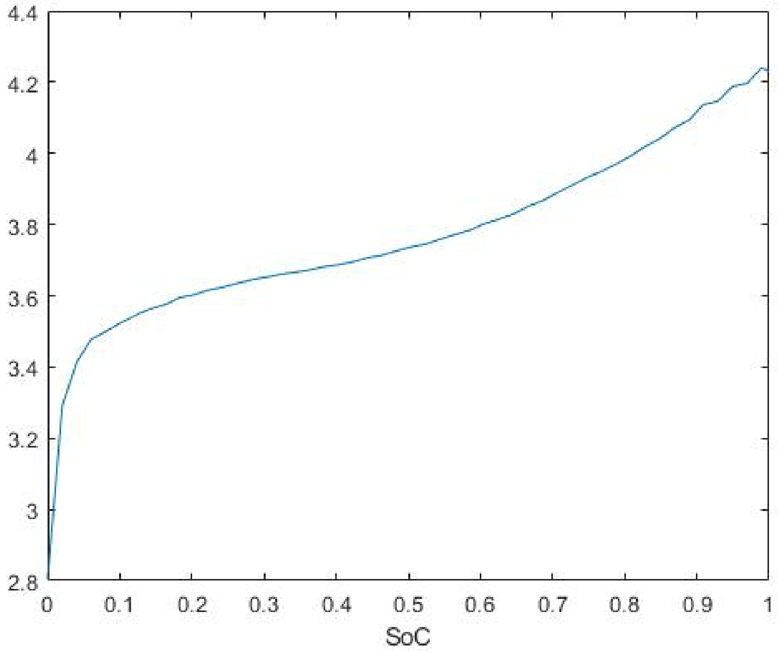

Figure 5.11: State of Charge (SOC) versus voltage curve for the battery during charge.

5.5.5 Discussion on Rint and Thevenin Models

Rint model, including equivalent series resistance: *Polarization refers to any departure of the cell's terminal voltage away from OCV due to a passage of current. For example, a cell's voltage drops when it is under load. This can be modelled in part as a resistance in series with the ideal voltage source (the Rint model).*

$$V(t) = OCV(z(t)) - i(t)R_0 \tag{5.11}$$

On charge: $V(t) > OCV(z(t))$

On discharge: $V(t) < OCV(z(t))$

Power dissipated by R_0 as heat leads to imperfect energy efficiency.

Diffusion Voltage: The Rint model suffices for simple electronics designs but not for advanced consumer electronics and XEV applications. The $i(t) \cdot R_0$ model gives an instantaneous response to a change in input current. In practice, we also observe a dynamic (non-instantaneous) response to a current step. Similarly, when the cell rests, voltage doesn't immediately return to OCV — it relaxes gradually. This is caused by the slow diffusion processes in the cell, so we refer to this slowly changing voltage as a diffusion voltage.

Thevenin Model Cell Voltage: Diffusion voltages can be closely approximated in a circuit using one or more parallel resistor-capacitor subcircuits. Cell voltage in the Thevenin model is:

$$V(t) = OCV(z(t)) - V_{C1}(t) - i(t)R_0 \tag{5.12}$$

To identify parameter values from test data, it's simpler to write the voltage in terms of element currents:

$$V(t) = OCV(z(t)) - R_1 i_{R1}(t) - R_0 i(t) \tag{5.13}$$

To find the expression for $i_{R1}(t)$, recognize that the current through R_1 plus the current through C_1 must equal $i(t)$. Further, $i_{C1}(t) = C_1 \frac{dV_{C1}(t)}{dt}$ which gives:

$$i_{R1}(t) + C_1 \frac{dV_{C1}(t)}{dt} = i(t) \tag{5.14}$$

$$V_{C1}(t) = R_1 i_{R1}(t) \tag{5.15}$$

$$i_{R1}(t) + R_1 C_1 \frac{di_{R1}(t)}{dt} = i(t) \tag{5.16}$$

$$\frac{di_{R1}(t)}{dt} = \frac{i(t) - i_{R1}(t)}{R_1 C_1} \tag{5.17}$$

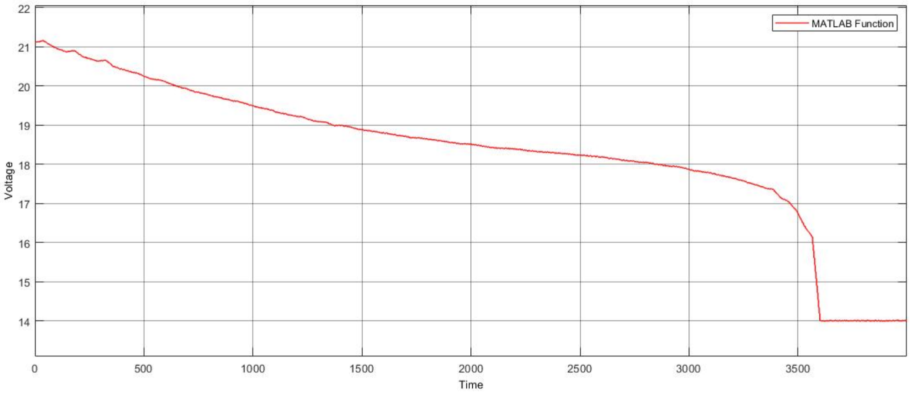

Figure 5.12: Simulated battery voltage (Vbatt) profile during discharge cycles.

To implement the control strategy, MATLAB Function Blocks were used. The following figures show the custom-written code for various components of the emulator model:

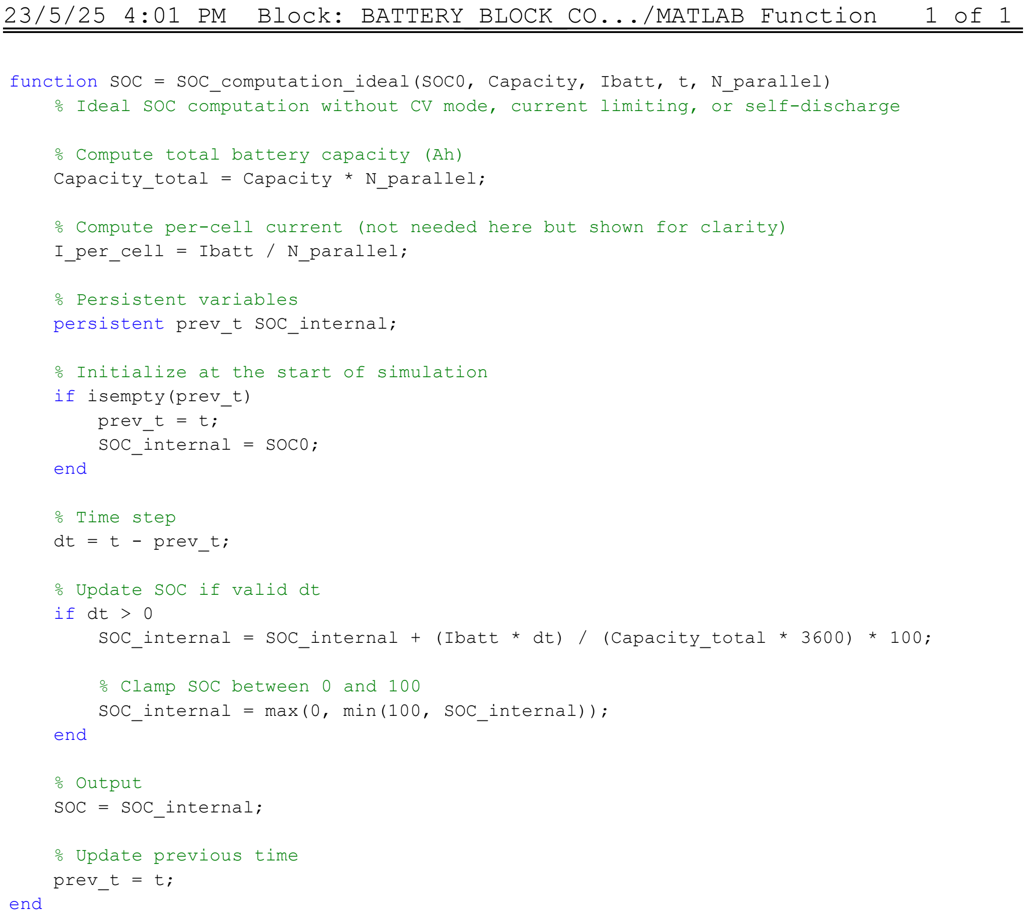

23/5/25 4:01 PM Block: BATTERY BLOCK CO.../MATLAB Function 1 of 1

```
function SOC = SOC_computation_ideal(SOC0, Capacity, Ibatt, t, N_parallel)
    % Ideal SOC computation without CV mode, current limiting, or self-discharge

    % Compute total battery capacity (Ah)
    Capacity_total = Capacity * N_parallel;

    % Compute per-cell current (not needed here but shown for clarity)
    I_per_cell = Ibatt / N_parallel;

    % Persistent variables
    persistent prev_t SOC_internal;

    % Initialize at the start of simulation
    if isempty(prev_t)
        prev_t = t;
        SOC_internal = SOC0;
    end

    % Time step
    dt = t - prev_t;

    % Update SOC if valid dt
    if dt > 0
        SOC_internal = SOC_internal + (Ibatt * dt) / (Capacity_total * 3600) * 100;

        % Clamp SOC between 0 and 100
        SOC_internal = max(0, min(100, SOC_internal));
    end

    % Output
    SOC = SOC_internal;

    % Update previous time
    prev_t = t;
end
```

Figure 5.13: MATLAB Function Block Code – SOC Estimation

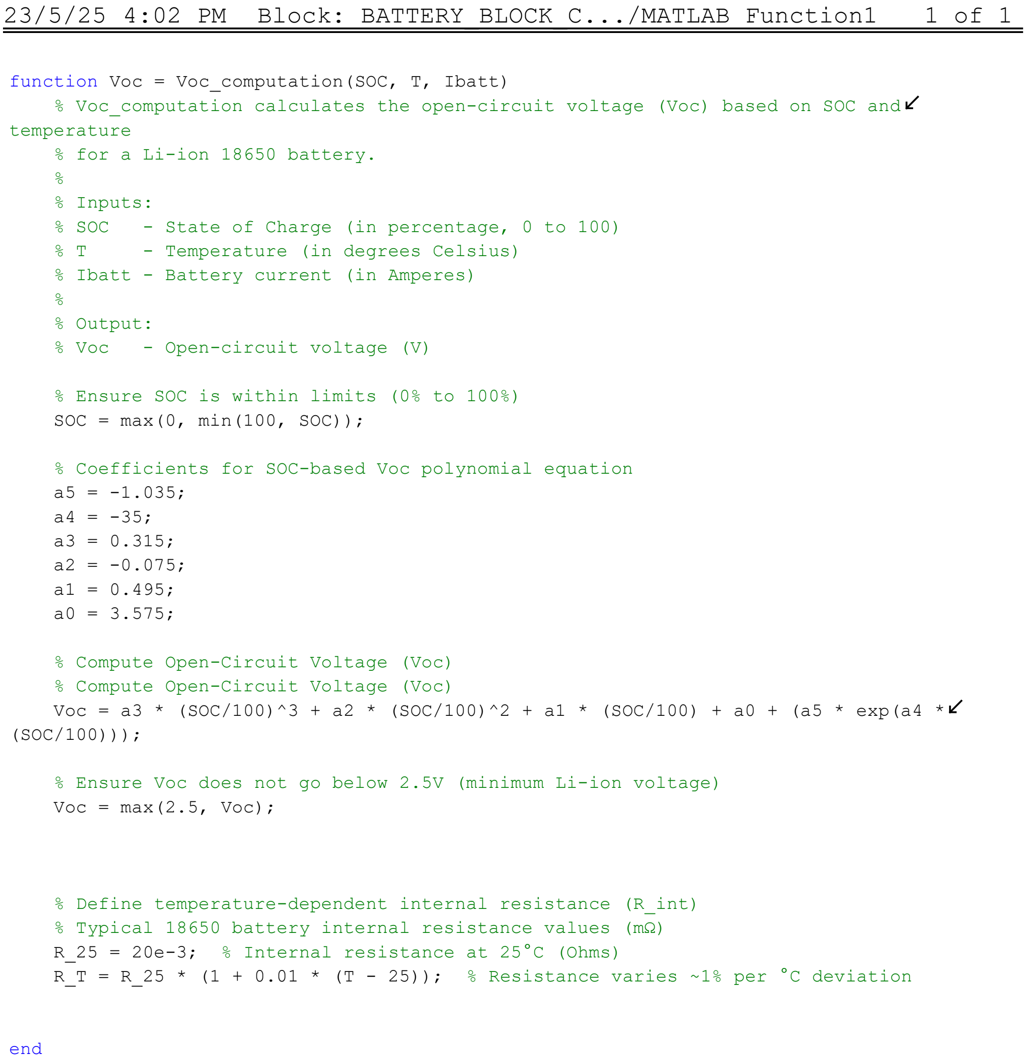

```
23/5/25 4:02 PM  Block: BATTERY BLOCK C.../MATLAB Function1   1 of 1

function Voc = Voc_computation(SOC, T, Ibatt)
    % Voc_computation calculates the open-circuit voltage (Voc) based on SOC and↙
temperature
    % for a Li-ion 18650 battery.
    %
    % Inputs:
    % SOC   - State of Charge (in percentage, 0 to 100)
    % T     - Temperature (in degrees Celsius)
    % Ibatt - Battery current (in Amperes)
    %
    % Output:
    % Voc   - Open-circuit voltage (V)

    % Ensure SOC is within limits (0% to 100%)
    SOC = max(0, min(100, SOC));

    % Coefficients for SOC-based Voc polynomial equation
    a5 = -1.035;
    a4 = -35;
    a3 = 0.315;
    a2 = -0.075;
    a1 = 0.495;
    a0 = 3.575;

    % Compute Open-Circuit Voltage (Voc)
    % Compute Open-Circuit Voltage (Voc)
    Voc = a3 * (SOC/100)^3 + a2 * (SOC/100)^2 + a1 * (SOC/100) + a0 + (a5 * exp(a4 *↙
(SOC/100)));

    % Ensure Voc does not go below 2.5V (minimum Li-ion voltage)
    Voc = max(2.5, Voc);



    % Define temperature-dependent internal resistance (R_int)
    % Typical 18650 battery internal resistance values (mΩ)
    R_25 = 20e-3;  % Internal resistance at 25°C (Ohms)
    R_T = R_25 * (1 + 0.01 * (T - 25));  % Resistance varies ~1% per °C deviation


end
```

Figure 5.14: MATLAB Function Block Code – Voltage Calculation

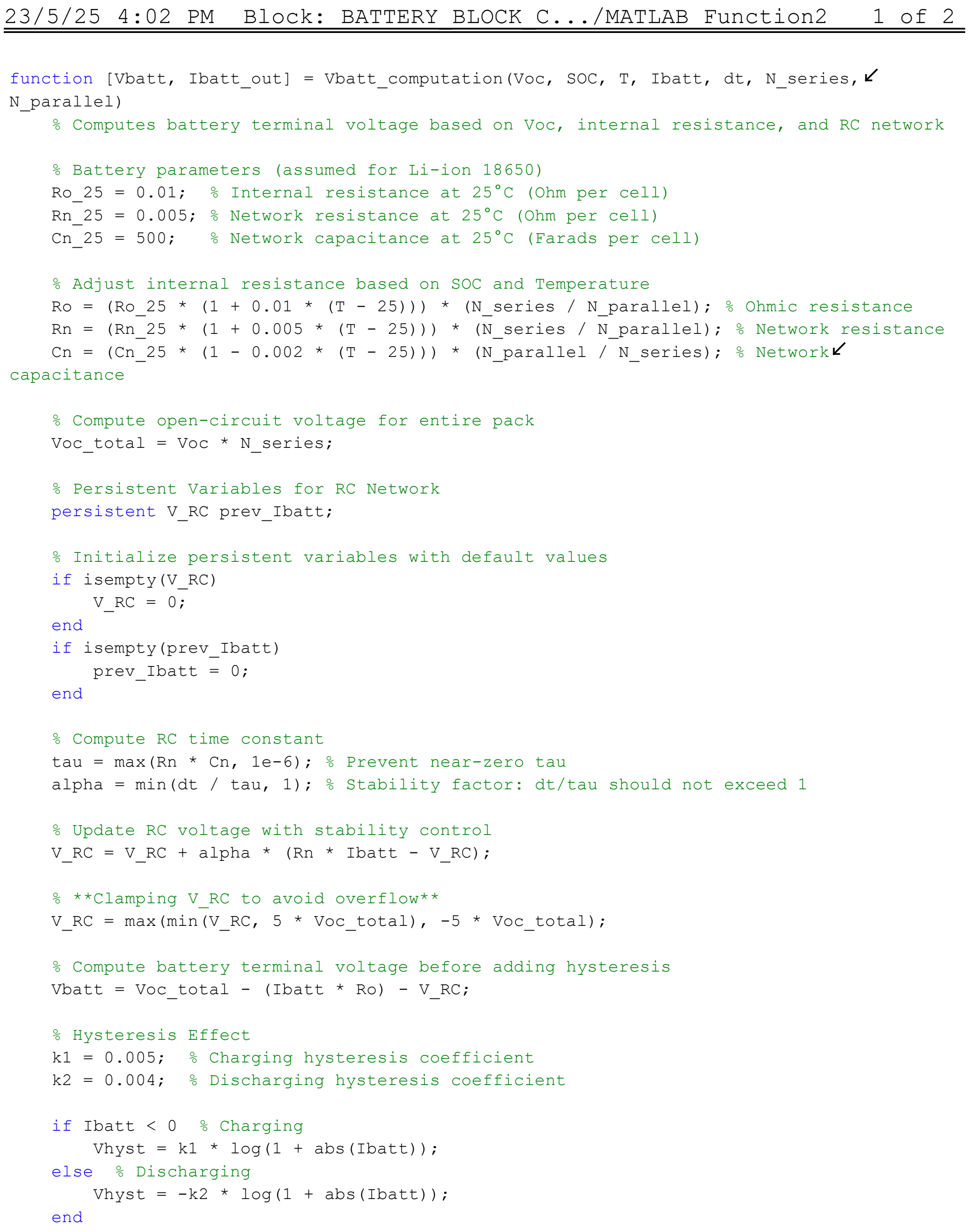

23/5/25 4:02 PM Block: BATTERY BLOCK C.../MATLAB Function2 1 of 2

```
function [Vbatt, Ibatt_out] = Vbatt_computation(Voc, SOC, T, Ibatt, dt, N_series,↙
N_parallel)
    % Computes battery terminal voltage based on Voc, internal resistance, and RC network

    % Battery parameters (assumed for Li-ion 18650)
    Ro_25 = 0.01;  % Internal resistance at 25°C (Ohm per cell)
    Rn_25 = 0.005; % Network resistance at 25°C (Ohm per cell)
    Cn_25 = 500;   % Network capacitance at 25°C (Farads per cell)

    % Adjust internal resistance based on SOC and Temperature
    Ro = (Ro_25 * (1 + 0.01 * (T - 25))) * (N_series / N_parallel); % Ohmic resistance
    Rn = (Rn_25 * (1 + 0.005 * (T - 25))) * (N_series / N_parallel); % Network resistance
    Cn = (Cn_25 * (1 - 0.002 * (T - 25))) * (N_parallel / N_series); % Network↙
capacitance

    % Compute open-circuit voltage for entire pack
    Voc_total = Voc * N_series;

    % Persistent Variables for RC Network
    persistent V_RC prev_Ibatt;

    % Initialize persistent variables with default values
    if isempty(V_RC)
        V_RC = 0;
    end
    if isempty(prev_Ibatt)
        prev_Ibatt = 0;
    end

    % Compute RC time constant
    tau = max(Rn * Cn, 1e-6); % Prevent near-zero tau
    alpha = min(dt / tau, 1); % Stability factor: dt/tau should not exceed 1

    % Update RC voltage with stability control
    V_RC = V_RC + alpha * (Rn * Ibatt - V_RC);

    % **Clamping V_RC to avoid overflow**
    V_RC = max(min(V_RC, 5 * Voc_total), -5 * Voc_total);

    % Compute battery terminal voltage before adding hysteresis
    Vbatt = Voc_total - (Ibatt * Ro) - V_RC;

    % Hysteresis Effect
    k1 = 0.005;  % Charging hysteresis coefficient
    k2 = 0.004;  % Discharging hysteresis coefficient

    if Ibatt < 0  % Charging
        Vhyst = k1 * log(1 + abs(Ibatt));
    else  % Discharging
        Vhyst = -k2 * log(1 + abs(Ibatt));
    end
```

Figure 5.15: MATLAB Function Block Code – Mode Switching Logic

Chapter 6

Hardware Topology and Circuit Design of Battery Emulator

6.1 Overview of the Hardware Architecture

The hardware architecture of the developed battery emulator comprises two main bidirectional power converter stages: an **Active rectifier** interfacing with the AC grid and a **bidirectional DC-DC converter** that emulates the behavior of the battery terminal.

The active rectifier draws power from the AC grid and regulates the intermediate DC link voltage. It also enables reverse power flow during charging conditions by operating as an inverter, thus maintaining the stability of the DC link.

The bidirectional DC-DC converter operates as a controlled voltage source using pulse-width modulation (PWM). It generates the terminal voltage V_{batt} based on the reference voltage $V_{\text{batt,ref}}$ computed in real time by the battery model. The converter supports two-quadrant operation, enabling both charging and discharging through the connected load. [14], [50]

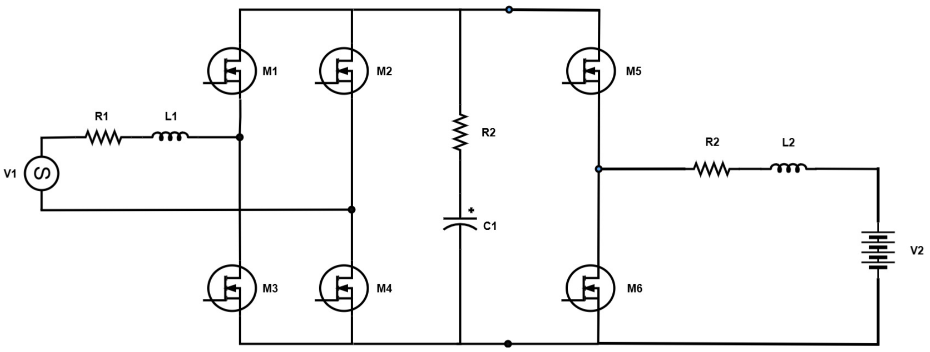

Figure 6.1: Full wave rectifier and Buck/Boost Converter with Battery. [14]

A DC-link capacitor C_{DC} acts as an energy buffer between the two converter stages, facilitating smooth power transfer. The emulator functions in the following modes:

- **Discharge Mode:** The active rectifier draws energy from the grid to maintain the DC-link voltage. The bidirectional converter steps this voltage down to supply the external load, effectively emulating battery discharge.
- **Charge Mode:** When the load injects current into the emulator, the bidirectional converter boosts the voltage and transfers the energy to the DC-link. The active rectifier, acting as an inverter, feeds this power back to the grid.

Protection mechanisms such as fuses and internal current limiting circuits are incorporated to ensure safe and reliable operation under abnormal or fault conditions.

6.2 DC/DC Bidirectional Converter Design

The HBC is specifically sized to support a 1C charge/discharge rate for the emulated battery pack, i.e., 11 A for an 11 Ah battery. The converter was designed considering both dynamic performance and efficiency, using a switching frequency of 25 kHz as a balance between control bandwidth and switching losses.

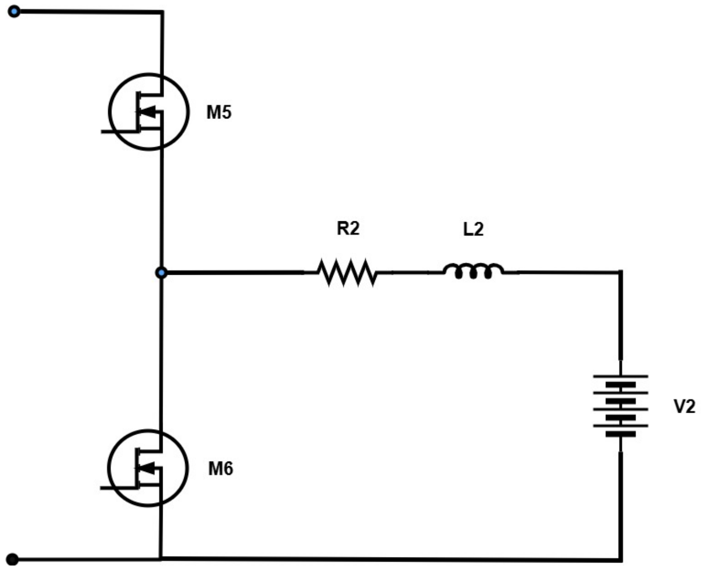

Figure 6.2: Buck Boost Bidirectional Converter. [15]

To minimize ripple while maintaining fast dynamic response, the output inductor (L) and capacitor (C) were selected based on the following design constraints:

- Output current ripple: $\leq 1\%$ of rated current
- Output voltage ripple: $\leq 1\%$ of rated voltage

The minimum required inductance and capacitance values were calculated using:

$$L_{\text{min}} = \frac{100 \cdot V_{\text{in}}}{8 \cdot f_{\text{sw}} \cdot I_{\text{out}} \cdot r_i} = 2\,\text{mH} \tag{6.1}$$

$$C_{\text{min}} = \frac{25}{L \cdot f_{\text{sw}}^2 \cdot r_v} = 2\,\text{mF} \tag{6.2}$$

However, higher values were selected in practice to ensure robustness under varying conditions [51] [14]. The final specifications of the Converter are given below:

Table 6.1: Electrical Parameters of the DC DC Converter

Parameter	Symbol	Value
Rated Power	P_N	1.22 kW
Input Voltage	V_{in}	400 V DC
Input Current	I_{in}	6 A DC
Output Voltage	V_{out}	100 V DC
Output Current	I_{out}	10 A DC
Output Inductor / Resistance	L, R_L	12 mH, 400 mΩ
Output Capacitor / Resistance	C, R_C	60 μF, 1.4 Ω
Switching Frequency	$f_{\text{sw,HBC}}$	25 kHz

6.2.1 Simulation Results

The experimental evaluation of the Converter under a 1C load condition (11 A) confirms its ability to deliver stable and regulated output. As shown in Fig. 6.3, the output voltage is maintained near 100 V, and the current remains within the 1% ripple constraint. The SOC profile reflects smooth charging/discharging behavior, validating effective integration with the battery simulator. These results confirm the suitability of the selected inductor and capacitor values, demonstrating reliable performance with good transient and steady-state response.

The measured output current of the DC-DC Converter, as shown in Figure 6.4, follows the expected charging profile with high fidelity. The current remains steady at 10 A with minimal ripple, well within the 1

The measured output voltage (V_{out}) closely follows the reference voltage (V_{ref}), demonstrating accurate voltage regulation and effective control. The minimal deviation between the two confirms the converter's fast dynamic response and steady-state accuracy.

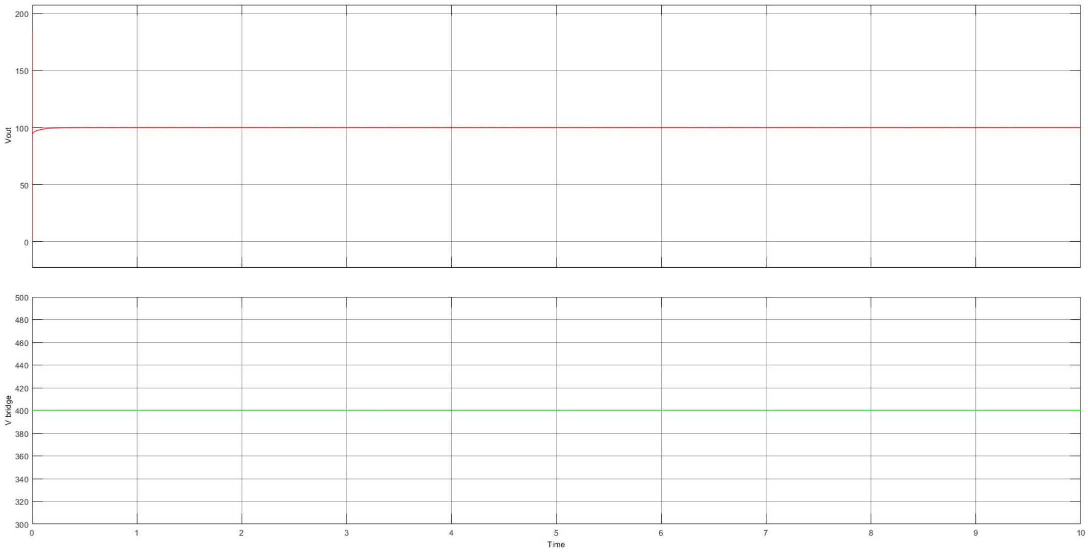

Figure 6.3: Measured output voltage (V_{out}) and (V_{Bridge}) under load.

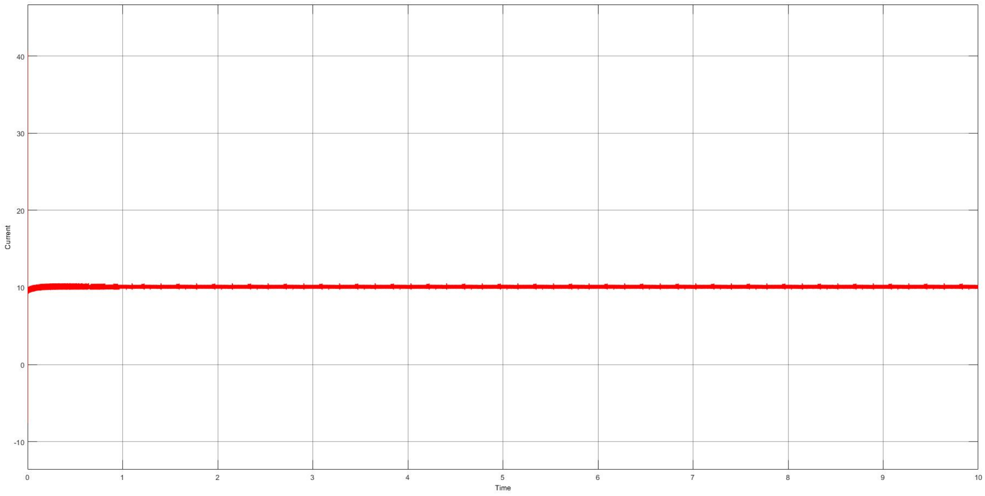

Figure 6.4: Measured output current (I_{out}).

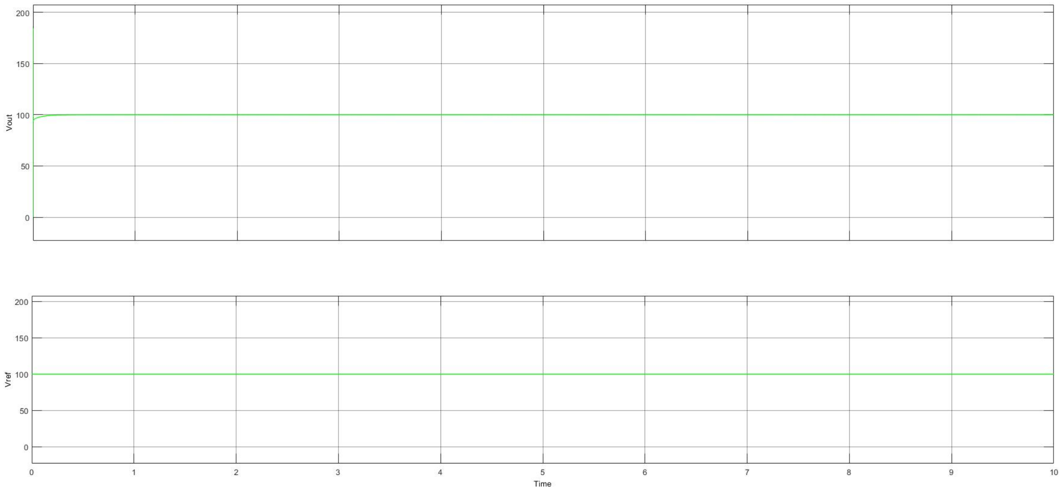

Figure 6.5: Measured output voltage (V_{out}) and reference voltage (V_{ref}) waveforms showing accurate tracking and stable regulation under load condition.

6.3 Single-Phase Active Rectifier

A single-phase active rectifier was implemented to interface with the AC mains, providing improved power quality and control compared to conventional diode rectifiers. Operating at a PWM switching frequency of 5 kHz, the active rectifier regulates energy flow from the AC source to the DC bus while maintaining a stable DC-link voltage. This configuration allows precise input current control, supports power factor correction, and ensures reliable operation of the downstream Half-Bridge DC-DC converter during simulated evaluation.[52]

When sizing the DC-link capacitor C_{DC}, the trade-off between ripple suppression and dynamic performance was considered. The minimum required capacitance can be estimated by:

$$C_{\text{DC}} \geq \frac{1}{32 \cdot r_{\text{DC,max}} \cdot L_R \cdot f_{\text{sw,VSI}}^2} \tag{6.3}$$

Table 6.2: Electrical Parameters of the Single-Phase VSI

Parameter	Symbol	Value
Rated Power	$P_{N,\text{VSI}}$	20 kW
AC Input Voltage (Grid)	$V_{\text{in, VSI}}$	230 V AC
AC Input Current	$I_{\text{in, VSI}}$	30 A RMS
Maximum DC Link Voltage	$V_{\text{DC, max}}$	400 V DC
DC Link Capacitance	C_{DC}	3000 μF
Switching Frequency	$F_{\text{sw, VSI}}$	10 kHz
Input Inductors	L_R	12 mH
Inductor Parasitic Resistance	R_R	300 mΩ

The RMS current through the DC-link capacitor is given by:

$$I_{DC,\text{ rms}} = \frac{V_{DC}}{8\sqrt{2} \cdot L_R \cdot f_{\text{sw, VSI}}} \tag{6.4}$$

Where:

- L_R is the AC-side inductance,
- $r_{\text{DC,max}}$ is the maximum acceptable ripple (typically 1%).

Film capacitors were preferred over electrolytic types due to their higher tolerance for ripple current, enabling a more compact and durable DC-link design. [53]

6.3.1 Simulation Results

The simulation confirms that the active rectifier maintains a stable DC-link voltage and delivers a sinusoidal input current. Figure 6.7 shows the input voltage and current waveforms, with a noticeable phase difference indicating potential for improved power factor correction.

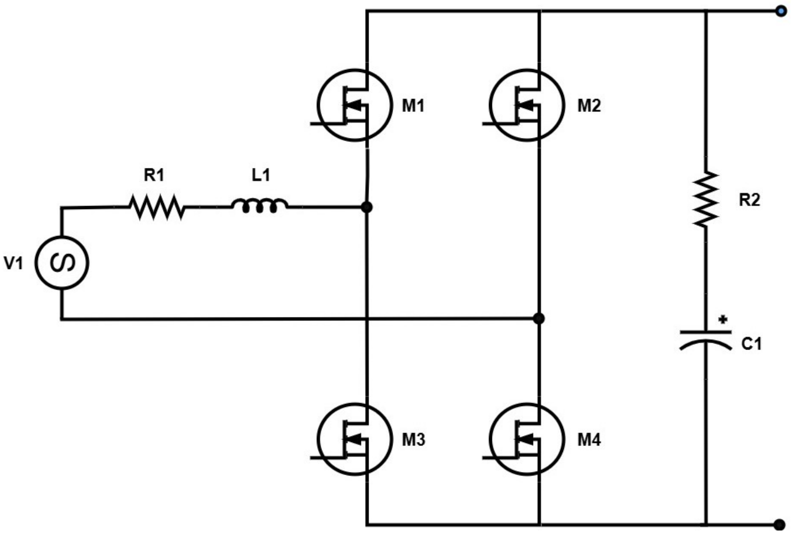

Figure 6.6: Active Rectifier. [14]

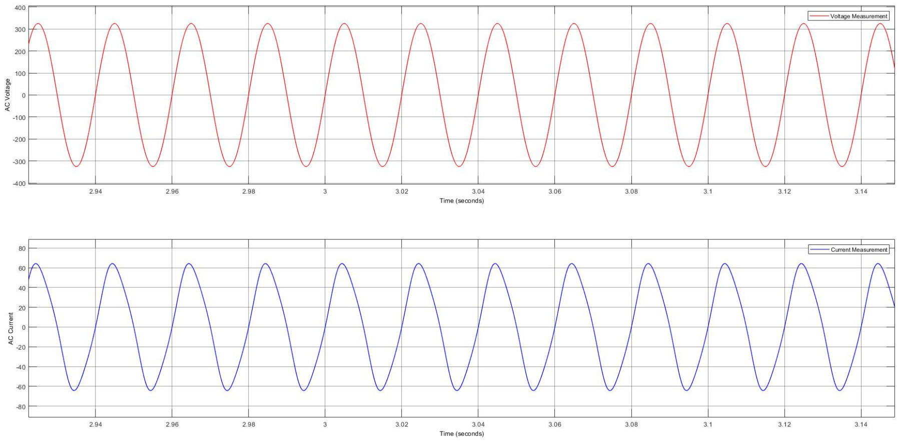

Figure 6.7: Simulated input voltage (V_{ac}) and current (I_{ac}) waveforms of the single-phase active rectifier.

Figure 6.8 illustrates the simulated DC-link voltage (V_{dc}) and current (I_{dc}) waveforms. The DC voltage remains stable around the desired reference, indicating effective voltage regulation. The output current shows expected dynamic behavior in response to load conditions, validating the control performance of the rectifier.

Cosine and sine reference signals are used to generate the modulation signals

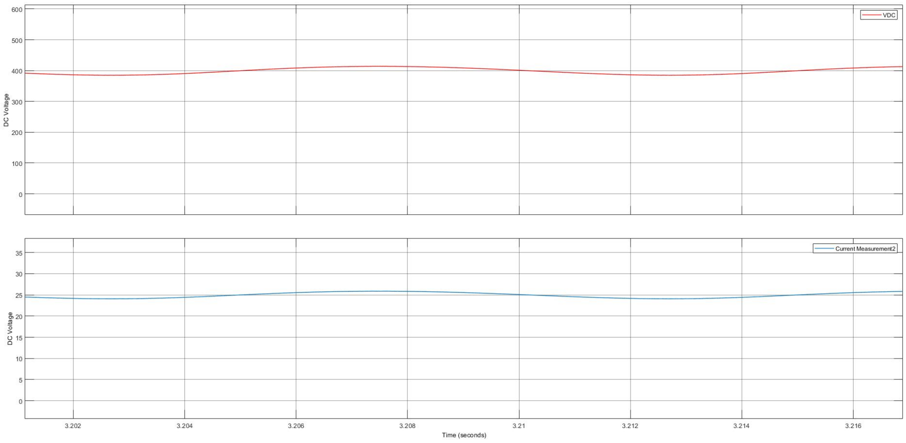

Figure 6.8: Simulated DC-link voltage (V_{dc}) and current (I_{dc}) waveforms of the single-phase active rectifier.

for the active rectifier. These waveforms ensure proper phase control and enable sinusoidal current shaping. Figure 6.9 shows the generated reference signals.

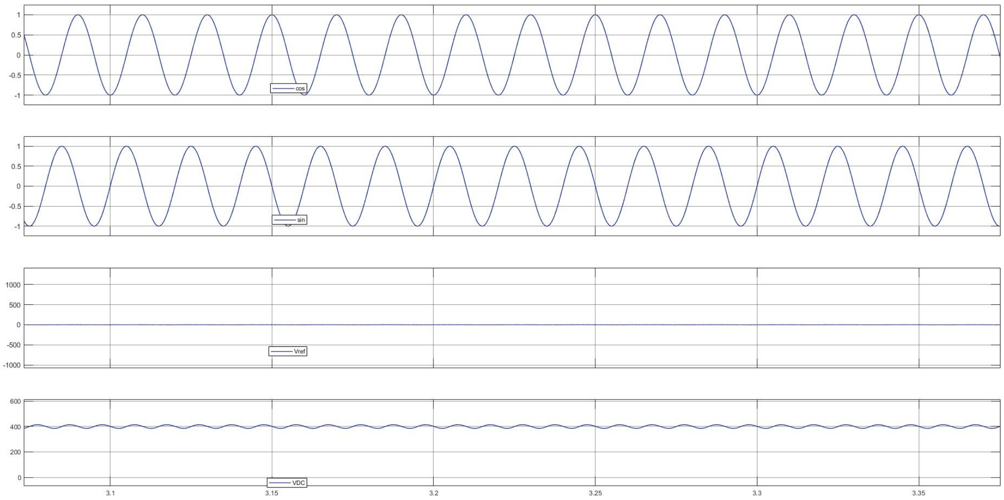

Figure 6.9: Generated cosine and sine reference signals for modulation.

PWM signals are generated by comparing the reference waveforms with a carrier signal to control the switching of the rectifier. Figure 6.10 presents the generated PWM signals.

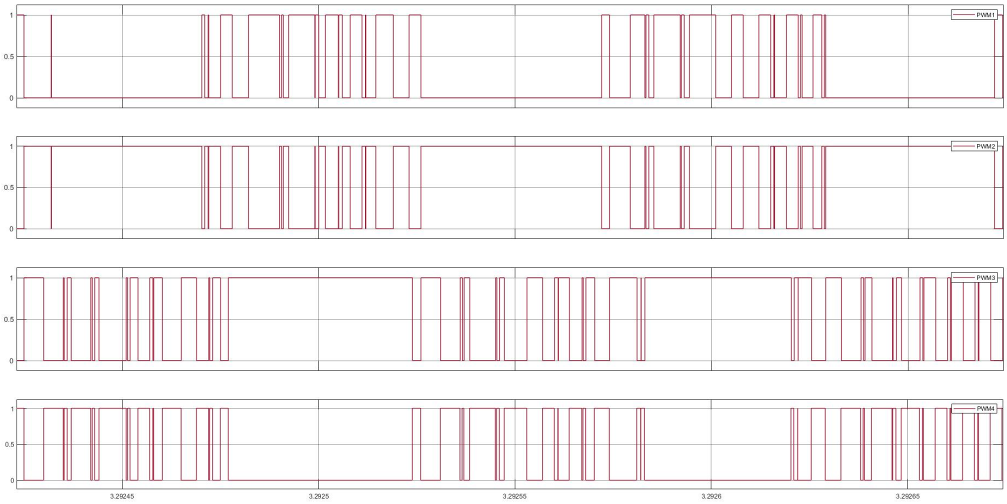

Figure 6.10: PWM signals used for switch control in the active rectifier.

6.4 Prototype Evaluation

No physical prototype was built; instead, the entire system was evaluated using MATLAB / Simulink simulations. The Converter and Active rectifier were modeled with realistic parameters, including a 400 V DC link voltage. The simulations showed effective control and decoupling of the converter stages, validating the proposed design.

The controller uses a PI feedback loop to regulate output voltage and ensure stable operation under varying loads.

6.5 Scalability Considerations

The proposed architecture can easily scale for higher-power applications. For ratings up to **100 kW**, it is feasible to redesign existing stages with appropriately rated components. For applications requiring even greater power, multiple emulator units can be connected in parallel. This modularity offers a clear ad-

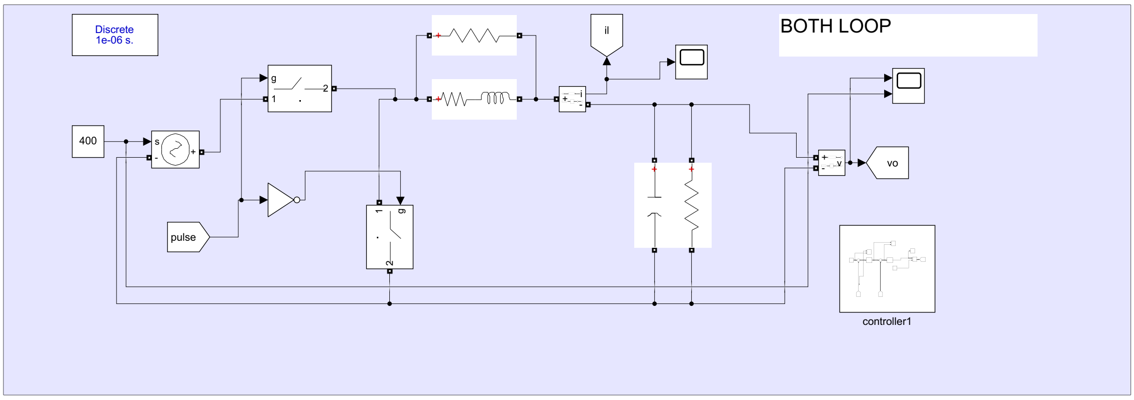

Figure 6.11: Simulink model diagram of the DC-DC converter used in the simulation study.

vantage over linear amplifiers, which typically suffer from low efficiency and are not suitable for high-power scenarios.

6.6 Grid Synchronization and Power Control Techniques

6.6.1 Phase-Locked Loop (PLL) Structure

To ensure synchronization with the grid, a **Phase Locked Loop (PLL)** is implemented in the control system. For this study, the **T/4 Delay PLL algo-**

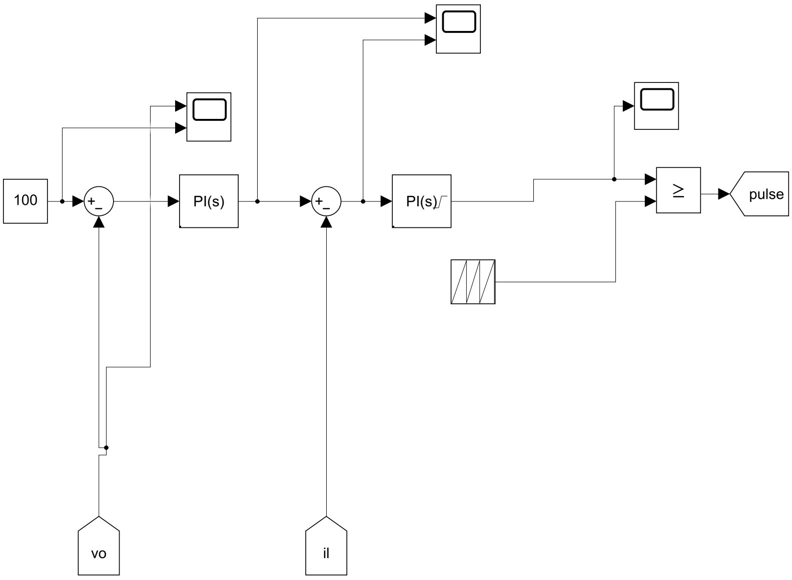

Figure 6.12: Block diagram of the controller implemented for the DC-DC converter.

rithm was adopted due to its effectiveness in handling grid-connected applications. [54]

This algorithm requires transformation between the stationary α-β **reference frame** and the rotating d-q **reference frame**. To generate the orthogonal β **component**, the real signal α is phase-shifted by 90° ($\pi/2$). In discrete time with sampling period T, this is achieved by delaying the α signal by $N = T/4$ samples.

The orthogonal component $\beta(n)$ can be expressed as:

$$\beta(n) = -\alpha(n - N) \tag{6.5}$$

From the α-β signals, the Park transformation produces the d-q components:

$$v_d(n) = \alpha(n)\cos(\theta(n)) + \beta(n)\sin(\theta(n)) \tag{6.6}$$

$$v_q(n) = -\alpha(n)\sin(\theta(n)) + \beta(n)\cos(\theta(n)) \tag{6.7}$$

The PLL error signal is defined as:

$$e(n) = v_d(n) \cdot v_q(n) \tag{6.8}$$

A proportional-integral (PI) controller acts on this error to adjust the estimated grid angle $\theta(n)$ and frequency $\omega(n)$:

$$\omega(n) = \omega(n-1) + K_p(e(n) - e(n-1)) + K_i e(n) \tag{6.9}$$

$$\theta(n) = \theta(n-1) + \omega(n)T \tag{6.10}$$

Here K_p and K_i are the gains of the PI controller.

6.6.2 Bidirectional Battery Charging/Discharging Control

The emulator supports bidirectional current flow that enables both charging and discharging of the emulated battery. Current direction and magnitude are managed by the control algorithms of the Converter and AC-DC converters, responding to the real-time battery model outputs. [15]

The hardware design, combined with software control, achieves rapid dynamic response and high efficiency during both energy injection and absorption phases.

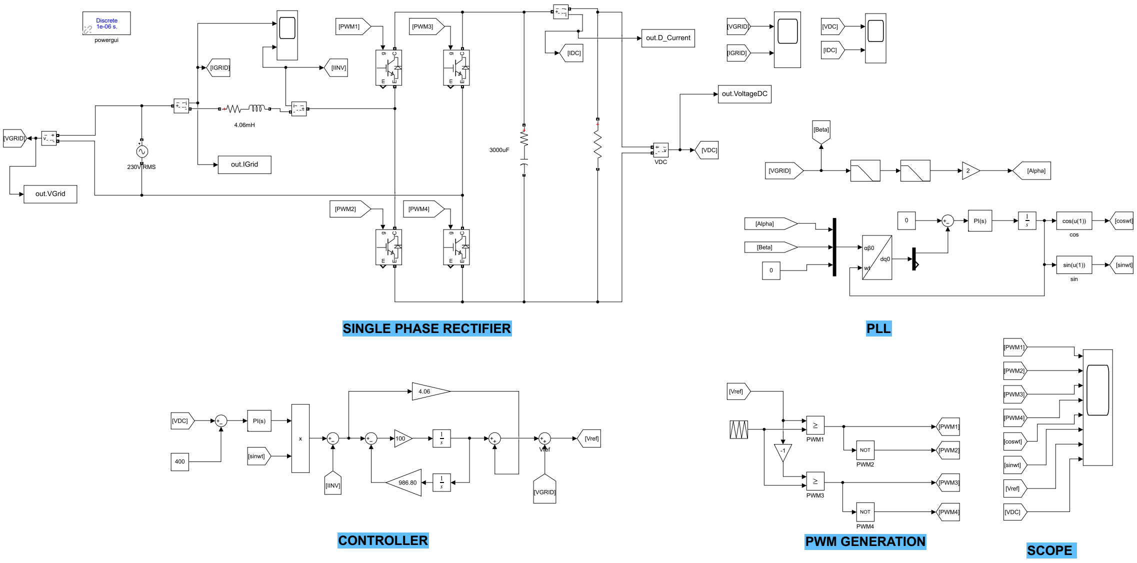

Figure 6.13: Diagram of the Active rectifier stage

6.7 Power Control Strategy and PR Current Controller

The control system of the grid-connected emulator uses a single-phase active rectifier with real-time power control and current regulation. The schematic of this system is shown in the control block diagram. Fig. 6.13

To monitor and regulate power flow, instantaneous active (P) and reactive (Q) power are calculated using the following expressions derived from $\alpha - \beta$ theory:

$$P = \frac{1}{2}(V_\alpha I_\alpha + V_\beta I_\beta) \tag{6.11}$$

$$Q = \frac{1}{2}(V_\alpha I_\beta - V_\beta I_\alpha) \tag{6.12}$$

These power values are compared against reference values, and the resulting error is processed by a PI controller. The corrected output is then used to compute the reference current.

The reference angle is calculated from the power ratio:

$$\theta_{ref} = \tan^{-1}\frac{Q}{P} \tag{6.13}$$

The corresponding q-axis reference current is computed by:

$$I_q = \frac{P}{V_g \cos(\theta_{ref})} \tag{6.14}$$

The final reference current injected into the grid becomes:

$$i_{ref} = 2I_q \sin(\omega t - \theta_{ref}) \tag{6.15}$$

This reference current is compared with the measured current I_α, and the resulting error is sent to the current controller.

6.8 Proportional Resonant (PR) Current Controller

The current control uses a Proportional Resonant (PR) controller, ideal for regulating sinusoidal currents in grid-tied systems without d-q transformation. Unlike an ideal PR controller with infinite gain at resonance, a non-ideal version with damping is employed to limit harmonic amplification. Its transfer function is:

$$G_{PR}(s) = K_p + \frac{2K_i s}{s^2 + 2\omega_c s + \omega_n^2} \tag{6.16}$$

where K_p is proportional gain, K_i integral gain, ω_n grid frequency, and ω_c damping cutoff. This ensures stable, fast, and accurate current control with harmonic rejection.

6.9 Bidirectional Battery Charger Circuit and Control Scheme

Bidirectional battery chargers play a vital role in modern energy storage systems, especially in electric vehicles, renewable energy integration, and microgrid applications. These systems must efficiently manage energy flow in both directions — charging the battery from a power source and discharging energy back to the load or grid. To achieve high efficiency and compact design, bidirectional DC-DC converters are commonly employed.

The converter topology used in this project consists of a single voltage source, a low-pass LC filter, two MOSFET switches, and a rechargeable battery. This simple yet effective circuit allows bidirectional current flow through controlled switching and energy storage components. The converter operates as a buck converter during battery charging and as a boost converter during discharging, depending on the power flow direction and switch states.

6.9.1 Battery Charging Operation: Buck Mode

During the charging phase, the converter steps down the input voltage and supplies a regulated current to the battery. This operation is essentially that of a buck converter. Two distinct switching intervals define the charging behavior:

In the first interval, often referred to as Mode-I, switch M1 is turned ON while M2 remains OFF. Under these conditions, both freewheeling diodes are non-conducting. The input supply is directly connected to the inductor and battery, causing the inductor current to increase linearly as energy is stored magnetically. This interval corresponds to the time when the PWM signal is high (from 0 to $D \cdot T$, where D is the duty cycle and T is the switching period).

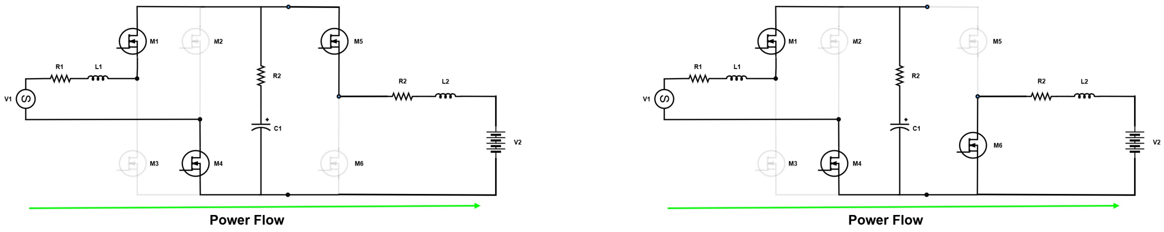

(a) Switches M1, M4, M5

(b) Switches M1, M4, M6

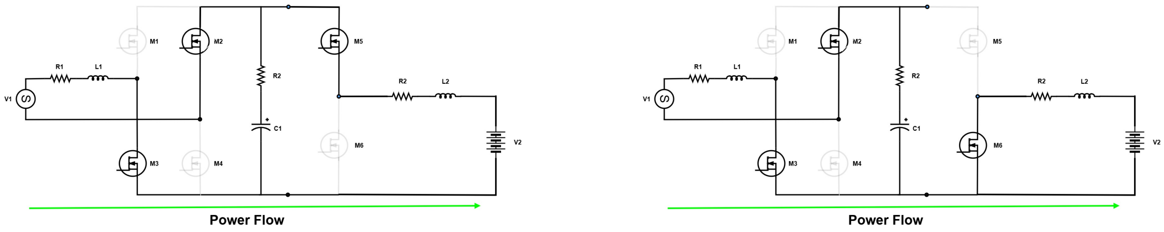

(c) Switches M2, M3, M5

(d) Switches M2, M3, M6

Figure 6.14: Switching cycle during Buck Mode.

In the second interval (Mode-II), both switches M5 and M6 are turned OFF. The energy stored in the inductor is now released to the battery through diode D6, maintaining a continuous current path. This freewheeling mode ensures the output current remains nearly constant, reducing stress on the battery and improving charge quality.

The average output voltage in buck mode is determined by the duty cycle and input voltage, as given by:

$$V_0 = \frac{t_{on}}{T} V_s \tag{6.17}$$

or equivalently,

$$V_0 = DV_s \quad \left(\because D = \frac{t_{on}}{T}\right) \tag{6.18}$$

This equation illustrates that by modulating the duty cycle D, the controller can regulate the voltage supplied to the battery with high precision. The resulting current waveform exhibits a controlled ramp-up and ramp-down behavior across switching cycles, as visualized in the standard charging mode waveforms. The inductor current oscillates between a minimum (I_1) and maximum (I_2) value, while the average output current remains stable due to the smoothing effect of the capacitor.

6.9.2 Battery Discharging Operation: Boost Mode

When the system operates in discharging mode, the converter topology transitions into a boost converter configuration. In this mode, the battery acts as the energy source, and power is delivered to the external load or system supply.

The discharging process is also divided into two operational intervals. During Mode-III, switch M6 is turned ON while M5 is kept OFF. The battery current flows through the inductor, charging it magnetically. Both freewheeling diodes remain non-conducting during this stage, and no energy is transferred to the load yet.

In Mode-IV, both switches are OFF, and diode D1 becomes forward-biased. The inductor releases its stored energy through the diode into the load. This results in a boost of the battery voltage, as energy from the inductor adds to the battery voltage at the output.

The average output voltage during boost operation is given by:

$$V_0 = \frac{1}{1-D} V_s \quad \left(\because D = \frac{t_{on}}{T}\right) \tag{6.19}$$

This expression shows that as the duty cycle increases, the output voltage rises, allowing the system to deliver higher voltages than the battery's nominal rating. Proper control of the duty cycle ensures safe and efficient energy transfer from the battery, especially in grid-tied or high-voltage systems.

The corresponding current waveforms in discharging mode show the inductor current increasing and decreasing symmetrically, similar to charging operation, but in the reverse direction. These controlled waveforms help maintain smooth power delivery and reduce electromagnetic interference.

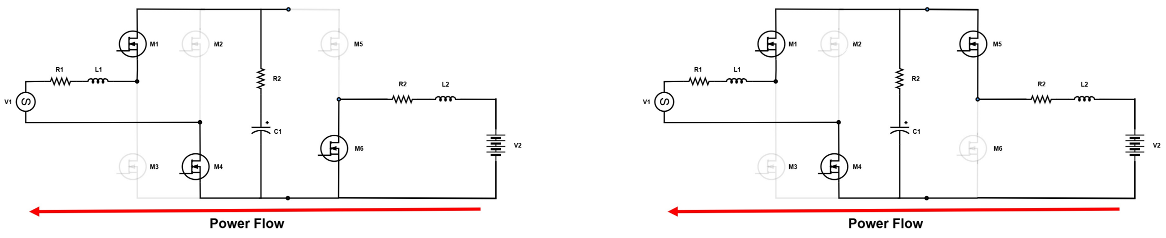

(a) Switches M1, M5, M6

(b) Switches M1, M4, M5

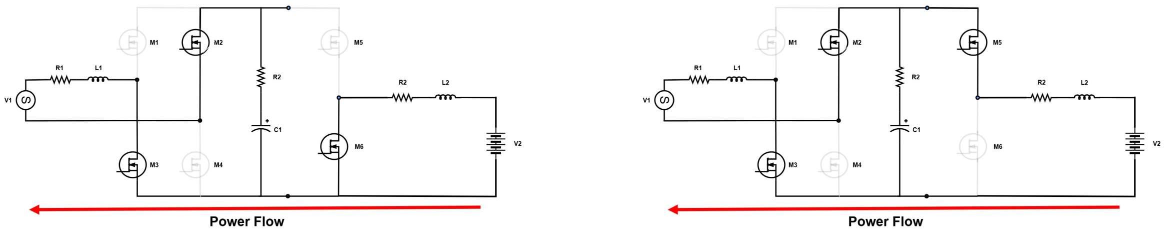

(c) Switches M2, M3, M6

(d) Switches M2, M3, M5

Figure 6.15: Switching cycle during Boost Mode.

6.10 Control Strategy for Bidirectional Operation

To ensure accurate and responsive control of current flow during both charging and discharging, a closed-loop feedback control system is implemented. The core of the control scheme relies on a Proportional-Integral (PI) controller paired with a PWM generator.

The system operates by continuously comparing the actual inductor current with a predefined reference current. This comparison generates an error signal, which is processed by the PI controller. The output of the controller modulates the duty cycle of the PWM signal, which in turn drives the gate signals of switches S5 and S6.

Depending on the desired mode of operation:

- In charging mode, PWM1 activates switch M5, and switch M6 remains OFF.
- In discharging mode, PWM2 activates switch M6, while switch M5 is turned OFF.

This logical switching ensures proper directionality of energy flow and maintains system stability under dynamic conditions. The use of a PI controller enables tight current regulation with minimal steady-state error, while the PWM generator allows for high-resolution control of the power electronic switches.

The overall scheme ensures that the converter can adaptively and efficiently manage the transitions between buck and boost modes, with reliable performance across different load scenarios and battery states.

6.11 Conclusion

In summary, the bidirectional DC-DC converter circuit provides a compact and flexible solution for managing both charging and discharging cycles in energy storage systems. Its ability to operate in both buck and boost configurations using a simple dual-switch structure makes it highly suitable for modern applications, including battery emulation, electric vehicle charging, and smart grid interfaces.

The integrated PI-based control scheme further enhances the performance by ensuring accurate current control and seamless mode switching. Together, the power stage and control system provide a foundation for reliable, high-efficiency bidirectional power conversion essential in advanced battery management and testing applications.

6.12 Dual Loop Control of Bidirectional DC-DC Buck-Boost Converter

Bidirectional DC-DC converters have gained significant importance in modern power electronics, especially in applications such as battery energy storage systems, renewable energy integration, and electric vehicles. Among various topologies, the buck-boost bidirectional converter is highly versatile as it can operate in both step-down (buck) and step-up (boost) modes, ensuring voltage regulation in both directions of power flow. However, maintaining stability and dynamic performance across varying operating conditions poses a control challenge.

To address these challenges, dual-loop control has emerged as an effective technique that improves both transient response and steady-state accuracy. In a dual-loop control structure, two control loops are employed:

- **Inner Loop (Current Control Loop)**: This loop regulates the inductor current and ensures fast response and protection against overcurrent conditions.
- **Outer Loop (Voltage Control Loop)**: This loop regulates the output voltage by generating the reference current for the inner loop.

Operation Principle

In the buck mode, the converter steps down the input voltage to a lower output voltage. In the boost mode, it increases the input voltage. The bidirectional nature allows seamless transition between charging and discharging modes in energy storage applications.

For such converters, the state-space averaged model provides the basis for control design. Considering a simplified non-isolated buck-boost converter, the voltage-current relationships in continuous conduction mode (CCM) can be expressed as:

6.13 Operation Principle

In the buck mode, the converter steps down the input voltage to a lower output voltage. Conversely, in the boost mode, it increases the input voltage. The bidirectional nature of the converter allows a seamless transition between charging and discharging modes in energy storage applications.

For such converters, the state-space averaged model provides the basis for control design. Considering a simplified non-isolated buck-boost converter operating in continuous conduction mode (CCM), the voltage-current relationships can be expressed as follows:

$$V_{out} = \begin{cases} D \cdot V_{in}, & \text{Buck mode} \\ \frac{V_{in}}{1-D}, & \text{Boost mode} \end{cases} \tag{6.20}$$

where D is the duty cycle, V_{in} is the input voltage, and V_{out} is the output voltage.

In the dual-loop control strategy, the outer voltage loop compares the measured output voltage V_{out} to the reference voltage V_{ref} and generates a reference current I_{ref} as:

$$I_{ref} = K_v \cdot (V_{ref} - V_{out}) \tag{6.21}$$

Here, K_v is the proportional-integral (PI) gain of the voltage controller.

This reference current I_{ref} is then used by the inner current loop, which compares it to the measured inductor current I_L. The resulting error is processed by another PI controller to produce the duty cycle D for the PWM control signal:

$$D = f(K_i \cdot (I_{ref} - I_L)) \tag{6.22}$$

where K_i is the PI gain of the current controller, and $f(\cdot)$ represents the PWM modulation function.

6.14 Advantages of Dual Loop Control

- **Improved Transient Response:** The inner current loop provides a fast dynamic response to disturbances, ensuring quick correction of current deviations.
- **Enhanced Stability:** The separation of time scales between the slower outer voltage loop and the faster inner current loop enhances overall system stability and robustness.
- **Robustness to Load Variations:** The inner current loop acts as a buffer, making the system less sensitive to sudden load changes and maintaining steady output voltage.
- **Bidirectional Operation:** The same dual-loop control structure can be effectively adapted to manage both charging (buck mode) and discharging (boost mode) operations, facilitating seamless bidirectional power flow.

Chapter 7

Conclusion and Future Work

7.1 Conclusion

This thesis has explored the modeling and emulation of Lithium-ion Batteries (LIBs), with a specific focus on empirical techniques and real-time implementation. Several key conclusions can be drawn from the work presented in the previous chapters:

The motivation for selecting LIBs as a core energy storage medium was discussed in Chapter 2, emphasizing their high energy density, scalability, and suitability for both high-power and high-energy applications. Although LIBs are currently associated with high costs, projections indicate a significant reduction in cost as manufacturing processes improve and economies of scale take effect [55]. Alternatives such as Sodium-Sulfur (Na-S) and Vanadium Redox (VR) flow batteries were also acknowledged for their potential in stationary storage applications, particularly for long-duration and large-scale energy requirements [2].

In Chapter 3, a comparative analysis of prevailing LIB chemistries was conducted. Among these, Lithium Iron Phosphate (LFP) emerged as a favorable candidate due to its thermal stability, long lifecycle, and relatively lower cost [5]. However, chemistries like Lithium Nickel Cobalt Aluminum Oxide (NCA), Lithium Nickel Manganese Cobalt Oxide (NMC), and Lithium Titanate Oxide (LTO) also exhibit promising capabilities, though their adoption is currently limited by cost and availability of raw materials. Novel chemistries such as lithium-silicon anodes were briefly reviewed, presenting interesting prospects for future energy-dense solutions [48].

Prior to the modeling phase, Chapter 4 presented a comprehensive review of battery behavior, including the effects of C-rate, temperature, and aging. These parameters significantly influence battery performance and underline the complexity of accurate modeling.

Chapter 5 offered a literature review of existing battery modeling methodologies. Empirical and semi-empirical models, such as the Shepherd model, offer a reasonable balance between computational simplicity and accuracy when operating within specified ranges [56]. However, their dynamic performance is often limited due to oversimplified assumptions and lack of non-linear behaviors.

In Chapter 6, the hardware topology and circuit design of the battery emulator were presented, highlighting the roles of the active rectifier and the bidirectional DC-DC converter. The active rectifier ensures regulated DC link voltage and supports bidirectional power flow, while the DC-DC converter accurately emulates battery terminal behavior using reference voltages from the battery model.

The overall design offers a reliable and flexible platform for real-time battery emulation, laying the groundwork for experimental validation in the subsequent chapter.

7.2 Future Work Recommendations

The following recommendations are proposed to further improve the accuracy and applicability of the Curve Fitting Model:

- **Validation with Real Battery Data:** Conduct a rigorous comparison between simulated results and measurements obtained from actual LIB cells under various load profiles.
- **Dynamic Voltage Modeling:** Incorporate a more detailed dynamic voltage response (especially V_{BOUT}) to enhance realism under transient conditions.
- **Constant Voltage (CV) Charging Phase:** Integrate modeling of the final charging phase using the concept of virtual impedance to improve emulation during tapering current scenarios.
- **State-of-Charge (SOC) Estimation Improvements:** Implement advanced SOC estimation algorithms such as Extended Kalman Filter (EKF), Unscented Kalman Filter (UKF), or machine learning techniques [23].
- **Incorporation of State-of-Health (SOH) and Aging Effects:** Introduce modules that account for battery degradation over time to estimate SOH and remaining useful life (RUL).
- **Temperature Feedback Loop:** Develop a temperature feedback mechanism that adjusts the model in real time based on thermal conditions.
- **Precision Optimization:** Explore different IQmath ranges and data quantization techniques to improve numerical stability and model fidelity in fixed-point environments.

In addition, close monitoring of trends in the LIB market and ongoing technological advancements will be essential. The industry is rapidly evolving, and it remains to be seen which LIB technology will ultimately dominate in terms of efficiency, cost, and safety.

Bibliography

[1] J. Leadbetter and L. G. Swan, “Selection of battery technology to support grid-integrated renewable electricity,” *Journal of Power Sources*, vol. 216, pp. 376–386, 2012.

[2] SIEMENS AG, “Siemens siestorage - the modular energy storage system for a reliable power supply.” `https://new.siemens.com/global/en/products/energy/medium-voltage/energy-automation-and-smart-grid/siestorage.html`, 2014. Accessed: 2025-05-24.

[3] H. Budde-Meiwes, J. Drillkens, B. Lunz, J. Muennix, S. Rothgang, J. Kowal, and D. U. Sauer, “A review of current automotive battery technology and future prospects,” *Journal of Energy Storage Technologies*, 2013. Exact publication details (journal name, volume, pages) were not provided—please update if known.

[4] SAMSUNG SDI, “Samsung sdi - energy storage system business presentation,” 2013.

[5] D. Anderson, “Status and trends in the hev/phev/ev battery industry.” `https://www.transportation.anl.gov/pdfs/B/582.PDF`, 2008. Accessed: 2025-05-24.

[6] lygte info.dk, “Nca battery - keeppower 18650 3600mah (black),” 2014. Online resource.

[7] A.-I. Stan, M. Swierczynski, D.-I. Stroe, R. Teodorescu, and S. J. Andreasen, “Lithium ion battery chemistries from renewable energy storage to automotive and back-up power applications; an overview,” in *Optimization of Electrical and Electronic Equipment (OPTIM), 2014 International Conference on*, pp. 713–720, May 2014.

[8] B. Kampman, M. Grünig, G. Duleep, and H. van Essen, “Assessment of electric vehicle and battery technology,” technical report, CE Delft, Delft, 2011.

[9] SAFT, “Lithium-ion battery life.” Technical document.

[10] Panasonic, “Storage energy system using lithium-ion batteries,” 2015. Technical brochure.

[11] LG Chem, “Advanced battery for energy storage system,” tech. rep., LG Chem, 2015.

[12] A. Hentunen, T. Lehmuspelto, and J. Suomela, “Time-domain parameter extraction method for thévenin-equivalent circuit battery models,” *IEEE Transactions on Energy Conversion*, vol. 29, pp. 558–566, September 2014.

[13] H. Chaoui, N. Golbon, I. Hmouz, R. Souissi, and S. Tahar, “Lyapunov-based adaptive state of charge and state of health estimation for lithium-ion batteries,” *IEEE Transactions on Industrial Electronics*, vol. 62, pp. 1610–1618, March 2015.

[14] E.-S. Kim, C.-J. Kim, and Y.-T. Kim, “Development of bidirectional ac-dc converter for energy storage systems,” in *2019 22nd International Confer-*

ence on Electrical Machines and Systems (ICEMS), pp. 1–4, 2019.

[15] W. Jianhua, Z. Fanghua, G. Chunying, and C. Ran, "Modeling and analysis of a buck/boost bidirectional converter with developed pwm switch model," in *8th International Conference on Power Electronics - ECCE Asia*, pp. 705–711, 2011.

[16] Office of Electricity Delivery U.S. Department of Energy and Energy Reliability, "Electric power industry needs for grid-scale storage applications," 2010.

[17] T. Mesbahi, N. Rizoug, P. Bartholomeus, and P. Le Moigne, "Li-ion battery emulator for electric vehicle applications," in *Vehicle Power and Propulsion Conference (VPPC), 2013 IEEE*, pp. 1–8, Oct. 2013.

[18] A. R. Sparacino, G. F. Reed, R. J. Kerestes, B. M. Grainger, and Z. T. Smith, "Survey of battery energy storage systems and modeling techniques," in *Power and Energy Society General Meeting, 2012 IEEE*, pp. 1–8, July 2012.

[19] MPOWER UK, "Nickel metal hydride batteries," 2014.

[20] M. Tamaki, K. Takagi, K. Shimada, N. Kawakami, and Y. Iijima, "Development of pcs for battery system installed in megawatt photovoltaic system," in *Power Electronics and Motion Control Conference (EPE/PEMC), 2012 15th International*, pp. LS1a–2.1–1–LS1a–2.1–4, Sept. 2012.

[21] A. Colthorpe, "A123 offshoot 24M targets us$100 per kwh costs for li-ion by 2020," *Energy Storage News*, 2015. Accessed online.

[22] Navigant Research, Sam Jaffe, "The lithium ion inflection point," 2013.

[23] I. Buchmann, “BU-205: Types of Lithium-ion.” `Battery University`, 2015. `https://batteryuniversity.com/article/bu-205-types-of-lithium-ion`.

[24] N. Nitta, F. Wu, J. T. Lee, and G. Yushin, “Li-ion battery materials: present and future,” *Materials Today*, vol. 18, no. 5, pp. 252–264, 2015.

[25] T. Fisher, “What goes into a tesla model s battery–and what it may cost,” 2015. Accessed online.

[26] Samsung SDI, “Samsung sdi - our next technology roadmap,” 2015.

[27] R. Rao, S. Vrudhula, and D. N. Rakhmatov, “Battery modeling for energy aware system design,” *Computer*, vol. 36, pp. 77–87, Dec. 2003.

[28] C. Zhang, K. Li, S. McLoone, and Z. Yang, “Battery modelling methods for electric vehicles - a review,” in *Control Conference (ECC), 2014 European*, pp. 2673–2678, June 2014.

[29] I. Buchmann, “BU-802b: Elevating Self Discharge.” `Battery University`, 2015. `https://batteryuniversity.com/article/bu-802b-elevating-self-discharge`.

[30] C. Simpson, “National instruments - characteristics of rechargeable batteries,” 2011.

[31] F. Hoffart, “Proper care extends li-ion battery life.”

[32] W.-Y. Chang, “The state of charge estimating methods for battery: A review,” *ISRN Applied Mathematics*, vol. 2013, p. 7, 2013.

[33] P.-H. Michel and V. Heiries, “An adaptive sigma point kalman filter hybridized by support vector machine algorithm for battery soc and soh es-

timation," in *Vehicular Technology Conference (VTC Spring), 2015 IEEE 81st*, pp. 1–7, May 2015.

[34] H. Rahimi-Eichi, U. Ojha, F. Baronti, and M. Chow, "Battery management system: An overview of its application in the smart grid and electric vehicles," *Industrial Electronics Magazine, IEEE*, vol. 7, pp. 4–16, June 2013.

[35] NEC Energy Systems, "Nec acquires grid energy storage and commercial systems business of a123 systems from wanxiang," 2014.

[36] M. T. Lawder, B. Suthar, P. W. C. Northrop, S. De, C. M. Hoff, O. Leitermann, M. L. Crow, S. Santhanagopalan, and V. R. Subramanian, "Battery energy storage system (bess) and battery management system (bms) for grid-scale applications," *Proceedings of the IEEE*, vol. 102, pp. 1014–1030, June 2014.

[37] C. M. Shepherd, "Theoretical design of primary and secondary cells, part iii - battery discharge equation," tech. rep., U. S. Naval Research Laboratory, 1963.

[38] S. Melentjev and D. Lebedev, "Overview of simplified mathematical models of batteries," in *13th International Symposium "Topical problems of education in the field of electrical and power engineering". Doctoral school of energy and geotechnology: Parnu, Estonia*, pp. 231–235, 2013.

[39] S. Wijewardana, "New dynamic battery model for hybrid vehicles," *International Journal of Emerging and Advanced Engineering*, vol. 4, no. 4, pp. 623–631, 2014.

[40] "Experimental validation of a battery dynamic model for ev applications," *World Electric Vehicle Journal*, vol. 3, pp. 1–10, 2009.

[41] The MathWorks, Inc., "Generic simulink battery model implementation," 2015.

[42] POWERSIM, "Psim tutorial - how to use lithium-ion battery model," 2013. Tutorial documentation.

[43] B. Schweighofer, K. M. Raab, and G. Brasseur, "Modeling of high power automotive batteries by the use of an automated test system," *Instrumentation and Measurement, IEEE Transactions on*, vol. 52, pp. 1087–1091, Aug. 2003.

[44] M. Chen and G. A. Rincon-Mora, "Accurate electrical battery model capable of predicting runtime and i-v performance," *IEEE Transactions on Energy Conversion*, vol. 21, pp. 504–511, June 2006.

[45] W. Y. Low, J. A. Aziz, P. Y. Kong, and N. R. N. Idris, "Modeling of lithium-ion battery using matlab/simulink," in *Industrial Electronics Society, IECON 2013 - 39th Annual Conference of the IEEE*, pp. 1729–1734, Nov. 2013.

[46] H. He, R. Xiong, and J. Fan, "Evaluation of lithium-ion battery equivalent circuit models for state of charge estimation by an experimental approach," *Energies*, vol. 4, no. 4, pp. 582–598, 2011.

[47] K. Sun and Q. Shu, "Overview of the types of battery models," in *Control Conference (CCC), 2011 30th Chinese*, pp. 3644–3648, July 2011.

[48] G. Aurilio, D. Gallo, C. Landi, M. Luiso, A. Rosano, M. Landi, and V. Paciello, "A battery equivalent-circuit model and an advanced technique for

parameter estimation," in *2015 IEEE International Instrumentation and Measurement Technology Conference (I2MTC)*, pp. 1705–1710, IEEE, May 2015.

[49] R. C. Kroeze and P. T. Krein, "Electrical battery model for use in dynamic electric vehicle simulations," in *Power Electronics Specialists Conference, 2008. PESC 2008. IEEE*, pp. 1336–1342, June 2008.

[50] K. R. Sreejyothi, Balakrishnakothapalli, K. Chenchireddy, S. A. Sydu, V. Kumar, and W. Sultana, "Bidirectional battery charger circuit using buck/boost converter," in *2022 6th International Conference on Electronics, Communication and Aerospace Technology*, pp. 63–68, 2022.

[51] S. Dash and M. Chandorkar, "Battery emulation using dual-active bridge converter," in *2019 National Power Electronics Conference (NPEC)*, pp. 1–6, 2019.

[52] S. Umesh, L. Venkatesha, and A. Usha, "Active power factor correction technique for single phase full bridge rectifier," in *2014 International Conference on Advances in Energy Conversion Technologies (ICAECT)*, pp. 130–135, 2014.

[53] K. Colak, E. Asa, and D. Czarkowski, "A novel phase control of single switch active rectifier for inductive power transfer applications," in *2016 IEEE Applied Power Electronics Conference and Exposition (APEC)*, pp. 1767–1772, 2016.

[54] H. He, Z. Li, T. Si, and L. Sun, "Research on digital phase locked method in pwm rectifier," in *2019 IEEE 8th Joint International Information Technology and Artificial Intelligence Conference (ITAIC)*, pp. 1866–1870, 2019.

[55] "Experimental validation of a battery dynamic model for ev applications," *World Electric Vehicle Journal*, vol. 3, pp. 1–10, 2009.

[56] D. Bazargan, S. Filizadeh, and G. Bistyak, "Battery characterization for vehicular applications using hardware-in-loop real-time simulation," in *2013 3rd International Conference on Electric Power and Energy Conversion Systems (EPECS)*, pp. 1–6, IEEE, October 2013.